Next Materials 11 (2026) 101966

Contents lists available at ScienceDirect

Next Materials

journal homepage: www.sciencedirect.com/journal/next-materials

Research article

Deoxygenation of waste corn oil over γ-Al_2O_3-supported Ni, Mo, and Ni–Mo catalysts for sustainable green diesel production

Karisma Pradina Putri [a], Muhammad Falila Izzuddin Haqq [a], Muhammad Naufal Alhilmy [a], Moh. Nadhif Mauluddin [b], A. Ghanaim Fasya [a,*], Susi Nurul Khalifah [a,*], Saidun Fiddaroini [c,*]

[a] Chemistry Study Program, Science and Technology Faculty, Universitas Islam Negeri Maulana Malik Ibrahim, Malang 65144, Indonesia
[b] Department of Chemistry, Faculty of Science, Chulalongkorn University, Bangkok 10330, Thailand
[c] Chemistry Department, Faculty of Mathematic and Natural Sciences, Brawijaya University, Malang 65144, Indonesia

ARTICLE INFO

Keywords:
Green diesel
Waste corn oil
Deoxygenation
Catalyst

ABSTRACT

Sustainable production of green diesel from waste feedstocks represents a promising strategy to address sustainability challenges in the global energy transition. This study evaluates the catalytic deoxygenation of waste corn oil over γ-Al_2O_3-supported monometallic and bimetallic catalysts under hydrogen-free conditions. Ni/γ-Al_2O_3 (10 wt% Ni), Mo/γ-Al_2O_3 (10 wt% Mo), and Ni–Mo/γ-Al_2O_3 (5 wt% Ni, 5 wt% Mo) catalysts were synthesized via wet impregnation followed by sonication, drying, and calcination. The catalysts were characterized using XRD, ATR-FTIR, N_2 adsorption–desorption, SEM–EDX, and ICP-OES. Deoxygenation reactions were conducted in a semi-batch reactor at 360 °C for 4 h under an inert N_2 atmosphere without external hydrogen. The waste corn oil feedstock, rich in C18 fatty acids, is suitable for producing diesel-range hydrocarbons. Among the tested catalysts, Ni–Mo/γ-Al_2O_3 achieved the highest liquid yield of 39.66%, representing a 22.2% increase relative to γ-Al_2O_3. The hydrocarbon content reached 91% (35.8% improvement), while diesel selectivity increased to 68% (41.7% enhancement). Paraffin selectivity also increased to 62%, representing a 3.3% improvement compared with γ-Al_2O_3. Catalyst reproducibility, reusability, and stability tests demonstrated that Ni–Mo/γ-Al_2O_3 retained stable catalytic performance over repeated reaction cycles, while thermogravimetric analysis (TGA) of the spent catalyst revealed carbon deposition as the main cause of catalyst deactivation. The superior performance of Ni–Mo/γ-Al_2O_3 originates from the synergistic interaction between NiO and MoO_3 species with complementary catalytic roles. NiO sites promote C–O bond cleavage through decarboxylation and decarbonylation pathways, whereas MoO_3 domains stabilize oxygenated intermediates and regulate secondary reactions such as cracking. This cooperative interaction enhances oxygen removal and favors the formation of diesel-range hydrocarbons under hydrogen-free conditions, highlighting the potential of Ni–Mo/γ-Al_2O_3 for sustainable green diesel production.

1. Introduction

The global transition from fossil fuels to renewable and low-carbon energy systems has become increasingly urgent in response to the long-term dependence on petroleum resources and the continued rise in greenhouse gas emissions. The energy sector accounts for more than 70% of anthropogenic CO_2 emissions worldwide, underscoring the critical role of the decarbonization of the energy system in climate change mitigation and long-term energy stability [1]. Despite substantial growth in renewable energy deployment over recent decades, fossil fuels still dominate the global primary energy mix, particularly in the transportation sector, which remains heavily dependent on petroleum-derived fuels [2]. Renewable liquid fuels such as green diesel have attracted substantial interest because catalytic deoxygenation of waste oil feedstocks yields paraffinic hydrocarbons with properties closer to those of petroleum diesel and can deliver lower lifecycle greenhouse gas emissions than conventional biodiesel, making them promising alternatives for decarbonizing transport fuels [3]. The development of renewable drop-in liquid fuels aligns with the Sustainable Development Goals related to affordable and clean energy (SDG 7),

* Corresponding authors.
E-mail addresses: fasya.organik@kim.uin-malang.ac.id (A.G. Fasya), susikhalifah@kim.uin-malang.ac.id (S.N. Khalifah), saidun@student.ub.ac.id, saidunfiddaroini99@gmail.com (S. Fiddaroini).

https://doi.org/10.1016/j.nxmate.2026.101966
Received 13 February 2026; Received in revised form 17 March 2026; Accepted 23 March 2026
Available online 25 March 2026

responsible consumption and production (SDG 12), and climate action (SDG 13), reinforcing their relevance to the sustainable energy transition [4].

Among the various biofuel options, green diesel has gained significant attention due to its chemical similarity to petroleum diesel, which consists primarily of saturated hydrocarbons with negligible oxygen content [5,6]. Unlike biodiesel, which retains oxygen in its molecular structure and exhibits lower oxidative stability, green diesel demonstrates higher cetane numbers, improved storage stability, and full compatibility with conventional diesel engines [6]. Technical assessments further indicate that green diesel possesses higher energy density and combustion characteristics more similar to those of fossil diesel than biodiesel, making it more suitable as a transitional low-carbon transportation fuel [7]. As a result, green diesel production not only meets transport fuel performance requirements but also helps reduce reliance on fossil fuels [8].

Green diesel is commonly produced through catalytic deoxygenation of triglycerides or fatty acids via hydrodeoxygenation (HDO), decarboxylation (DCO_2), and decarbonylation (DCO) pathways. The relative contribution of these reaction routes is strongly influenced by catalyst composition and reaction conditions [9]. Among these pathways, DCO and DCO_2 reactions are particularly attractive under hydrogen-free or hydrogen-lean conditions because they eliminate the need for an external high-pressure hydrogen supply, thereby reducing both capital costs and safety concerns associated with industrial-scale hydrogen infrastructure [7]. In hydrogen-lean systems, reactive hydrogen species may be generated in situ via secondary reactions, such as the water–gas shift reaction, thereby enabling partial saturation of intermediates without continuous hydrogen supply [9]. Previous studies have demonstrated that reaction pathway selectivity is strongly influenced by catalyst type, surface acidity, metal dispersion, and operating parameters. Therefore, rational catalyst design and feedstock selection play a decisive role in directing product selectivity toward diesel-range hydrocarbons during catalytic deoxygenation [9,59].

Feedstock selection is a critical factor in determining the overall sustainability and process efficiency of green diesel production pathways. The valorization of waste oils derived from agro-industrial supply chains enables the conversion of low-value residual streams into high-value transportation fuels without exerting additional pressure on edible oil markets, thereby supporting resource efficiency and aligning with Sustainable Development Goal 12 (Responsible Consumption and Production) [10]. Waste corn oil is predominantly composed of C18 fatty acids. Reported compositional analyses indicate that linoleic acid (C18:2) typically accounts for approximately 50–60 wt%, while oleic acid (C18:1) represents about 20–30 wt%, with palmitic acid (C16:0) commonly ranging between 8–12 wt% [11,12]. This high proportion of C18 unsaturated fatty acids is particularly advantageous for catalytic deoxygenation processes, as theoretical decarboxylation and decarbonylation pathways yield hydrocarbons in the C17 range, whereas hydrodeoxygenation yields C18 hydrocarbons, both falling within the diesel-range carbon window (C15–C20). The intrinsic fatty-acid profile of waste corn oil therefore makes it a compositionally suitable feedstock for green diesel production [9].

From a catalyst perspective, Ni-based catalysts are widely reported to be effective for C–O bond cleavage and hydrogen-transfer reactions in deoxygenation processes, offering strong activity for decarbonylation and decarboxylation routes under hydrogen-lean conditions. Recent reviews and experimental studies have summarized Ni-based systems for the selective deoxygenation of vegetable and waste oils [13]. γ-Al_2O_3 is commonly used as a support due to its high specific surface area, thermal stability, and ability to disperse active metal species; these attributes help improve catalyst performance in hydroprocessing and deoxygenation reactions [14,15]. Mo-based catalysts provide oxophilic sites that can facilitate oxygen removal and modify surface acidity. Mo-based catalysts used as promoters in bimetallic formulations have been shown to improve oxygen-removal efficiency and affect coke formation and product distribution [16]. Synergistic interactions between NiO and MoO_3 in Ni–Mo bimetallic systems supported on oxides (including γ-Al_2O_3) frequently exhibit enhanced activity, improved selectivity toward long-chain hydrocarbons, and greater catalyst stability compared with corresponding monometallic systems. Recent experimental and review articles document the synergistic interaction between Ni and Mo in hydroprocessing and deoxygenation of triglyceride-derived feedstocks [17].

Despite the extensive body of literature on Ni- and Mo-based catalysts in hydroprocessing applications, systematic head-to-head comparisons of monometallic NiO, MoO_3, and bimetallic Ni–Mo catalysts using waste corn oil (WCO) as a feedstock rich in C18 fatty acids remain scarce, particularly under consistent hydrogen-free conditions. In particular, the influence of metal composition on deoxygenation pathway selectivity and diesel-range hydrocarbon formation from waste corn oil under externally hydrogen-free conditions has not been comprehensively clarified. This study therefore aims to systematically investigate the deoxygenation performance of γ-Al_2O_3-supported Ni (10 wt%), Mo (10 wt%), and Ni–Mo (5 wt% Ni–5 wt% Mo) catalysts prepared via wet impregnation combined with sonication to enhance metal dispersion. Catalyst physicochemical properties, including crystalline structure, surface functional groups, textural characteristics, and metal distribution, were examined using XRD, ATR-FTIR, N_2 adsorption–desorption, ICP-OES, and SEM-EDX analyses. These data were correlated with catalytic metrics, including oil conversion, relative hydrocarbon content, diesel-range selectivity (C15–C20), and coke formation tendency under hydrogen-free deoxygenation in an inert N_2 atmosphere. In addition, catalytic reproducibility, reusability, and stability were evaluated through repeated reaction cycles using the Ni–Mo/γ-Al_2O_3 catalyst to assess catalyst durability under hydrogen-free conditions. Thermogravimetric analysis (TGA) of the spent Ni–Mo/γ-Al_2O_3 catalyst was further conducted to quantify carbon deposition and evaluate its contribution to catalyst deactivation. Through the direct comparison of mono- and bimetallic systems under identical conditions, this work elucidates how metal composition and metal–support interactions govern liquid yield, relative hydrocarbon content, hydrocarbon chain distribution, fuel-range selectivity, and paraffin–olefin distribution. The findings provide a clearer structure–performance impregnation for rational catalyst design in sustainable green diesel production from waste corn oil feedstocks

2. Methods

2.1. Materials

The materials used in this study included waste corn oil obtained from a local source in Indonesia, nickel(II) nitrate hexahydrate ($Ni(NO_3)_2{\cdot}6H_2O$, Merck, 99.99%), ammonium heptamolybdate tetrahydrate ($(NH_4)_6Mo_7O_{24}{\cdot}4H_2O$, Merck, 99.0%), commercial γ-Al_2O_3 (Merck, 99.99%), demineralized water (Waterbatt), n-hexane (Merck, 99%), and nitrogen gas (N_2, 99.999%).

2.2. Catalysts synthesis

Ni/γ-Al_2O_3, Mo/γ-Al_2O_3, and Ni–Mo/γ-Al_2O_3 catalysts were synthesized via an impregnation–sonication method adapted from procedures previously reported by Hongloi et al. (2019) [18] and Zepeda et al. (2025) [19]. The variation matrix and the corresponding amounts of metal precursors used for each catalyst formulation are presented in Table 1. For the monometallic catalysts, $Ni(NO_3)_2{\cdot}6H_2O$ (4.9530 g, corresponding to 10 wt% Ni) or $(NH_4)_6Mo_7O_{24}{\cdot}4H_2O$ (1.8400 g, corresponding to 10 wt% Mo) was dissolved in 50 mL of deionized water. For the bimetallic catalyst, $Ni(NO_3)_2{\cdot}6H_2O$ (2.4765 g, 5 wt% Ni) and $(NH_4)_6Mo_7O_{24}{\cdot}4H_2O$ (0.9200 g, 5 wt% Mo) were co-dissolved in the same volume of deionized water. The mass of metal precursor used for each catalyst was determined based on the targeted metal loading (wt%)

Table 1
Variation matrix synthesis of Ni/γ-Al_2O_3, Mo/γ-Al_2O_3, and Ni–Mo/γ-Al_2O_3 catalysts.

Catalyst Variation	Mass of ($Ni(NO_3)_2 \cdot 6H_2O$)	Mass of ($(NH_4)_6Mo_7O_{24} \cdot 4H_2O$)	Mass of γ-Al_2O_3
Ni/γ-Al_2O_3	4.9530 g	-	10 g
Mo/γ-Al_2O_3	-	1.8400 g	10 g
Ni–Mo/γ-Al_2O_3	2.4765 g	0.9200 g	10 g

relative to the support mass and adjusted according to the metal content and molecular weight of the precursor.

In all preparations, 10 g of γ-Al_2O_3 support was gradually added to the precursor solution under continuous magnetic stirring at room temperature, and the mixture was maintained for 2 h to ensure homogeneous impregnation. The resulting slurry was then subjected to probe sonication (Qsonica Q−500, 20 kHz, 40% amplitude, pulse 5 s on / 5 s off) for a total of 4 h (effective sonication time: 2 h). Ultrasonic treatment was applied to improve the dispersion of metal precursors within the porous structure of the support during the impregnation process. Subsequently, the samples were dried at 80 °C for 8 h and calcined at 550 °C for 5 h.

2.3. Catalyst characterization

2.3.1. XRD analysis

The crystalline phases of the synthesized catalysts were analyzed by a Bruker D8 Advance X-ray diffractometer equipped with Cu Kα radiation (λ = 1.5406 Å). Approximately 0.2–0.5 g of catalyst powder was finely ground and uniformly spread on a glass sample holder. Diffraction patterns were recorded over a 2θ range of 10°–90° with a scanning rate of 0.02° s^{-1} . Phase identification and preliminary data processing were performed using X'Pert HighScore software, followed by further data analysis using Origin software.

2.3.2. ATR-FTIR analysis

The functional groups and chemical bonding of the catalysts were examined using attenuated total reflectance Fourier transform infrared spectroscopy (ATR-FTIR) with a Shimadzu IRSpirit-T spectrometer. Spectra were collected in the range of 4000–400 cm^{-1} and processed using Origin software to identify characteristic vibrational bands associated with γ-Al_2O_3 and the impregnated metal species.

2.3.3. N_2 adsorption–desorption isotherm analysis

Textural properties, including specific surface area, pore volume, and pore size distribution, were determined by N_2 adsorption–desorption measurements using a Micromeritics 3Flex surface area and pore size analyzer. Prior to analysis, the samples were degassed under vacuum. The specific surface area was calculated using the Brunauer–Emmett–Teller (BET) method, while pore size distribution and pore volume were determined using the Barrett–Joyner–Halenda (BJH) method. The resulting data were processed and plotted using Origin software.

2.3.4. SEM–EDX analysis

Surface morphology, elemental composition, and elemental distribution of the catalysts were analyzed by scanning electron microscopy coupled with energy-dispersive X-ray spectroscopy (SEM–EDX) using a JEOL JSM-IT Series InTouchScope microscope. Approximately 10 mg of dried catalyst powder was mounted on an aluminum stub using carbon tape. SEM–EDX analysis was performed at an accelerating voltage of 20 kV. The acquired micrographs and elemental maps were processed and analyzed using ImageJ and Origin software.

2.3.5. ICP–OES analysis

The actual metal loading of Ni and Mo in the prepared catalysts was determined using Inductively Coupled Plasma–Optical Emission Spectroscopy (ICP–OES) (Thermo Scientific iCAP 6500). The sample preparation procedure followed the method reported by Ameen et al. (2020) [20]. Approximately 0.1 g of catalyst sample was dissolved in an aqueous HCl/HNO_3 solution and heated at 573.15 K in a sand bath to ensure complete dissolution of the metal species. The resulting solution was evaporated to dryness and subsequently re-dissolved in 3.4 mL HNO_3 and 10 mL of deionized water. The solution was then diluted from 1 mL to 15 mL prior to ICP–OES analysis. The concentrations of Ni and Mo were quantified and expressed as mass fractions (wt%), providing accurate determination of the actual metal loading in the catalysts. This analysis complements the EDX surface analysis, which primarily reflects the surface elemental distribution.

2.4. Preparation of waste corn oil

Before the deoxygenation reaction, the waste corn oil was purified by repeated washing with hot distilled water (70–80 °C) to remove residual impurities. The oil–water mixture was agitated and allowed to settle and separate, and the aqueous phase was then removed. This procedure was repeated until a clear oil phase was obtained.

2.5. Deoxygenation of waste corn oil

The deoxygenation reaction was carried out in a semi-batch system in a 100 mL three-neck flask equipped with a distillation setup, heating mantle, thermometer, and condenser, as shown schematically in Fig. 1. A total of 0.3 g of γ-Al_2O_3 catalyst was introduced into 10 g of waste corn oil, corresponding to a catalyst-to-feed ratio of 3 wt%. The mixture was stirred with a magnetic stirrer while N_2 gas was supplied. The reaction was conducted at 360 °C for 4 h. N_2 gas was continuously supplied throughout the reaction to maintain inert conditions. The vapor was condensed, and the collected liquid fraction was collected in a distillate flask. The liquid product and coke were then weighed using an analytical balance. The same procedure was repeated with Ni/γ-Al_2O_3, Mo/γ-Al_2O_3, and Ni–Mo/γ-Al_2O_3 catalysts. Liquid, coke, and gas yields were calculated using Eqs. (1), (2), and (3).

$$\text{Liquid yield}(\%) = \left(\frac{\text{mass of liquid product}}{\text{mass of feedstocks}}\right) \text{x}100 \quad (1)$$

$$\text{Coke yield}(\%) = \left(\frac{\text{mass of coke formed}}{\text{mass of feedstocks}}\right) \text{x}100 \quad (2)$$

$$\text{Gas yield } (\%) = 100 - (\text{liquid yield} + \text{coke yield}) \quad (3)$$

2.6. Coke analysis

2.6.1. ATR-FTIR analysis

Coke formed as a by-product during the deoxygenation reaction was separated together with the catalyst by filtration and subsequently washed repeatedly with n-hexane to remove residual liquid products. The solid samples were then dried at 80 °C for 12 h and finely ground. The chemical nature of the coke deposits was analyzed by attenuated total reflectance Fourier transform infrared spectroscopy (ATR-FTIR) using a Shimadzu IRSpirit-T spectrometer. Infrared spectra were recorded in the range of 4000–400 cm^{-1} and compared with those of the fresh catalysts to identify characteristic functional groups associated with carbonaceous species formed during the reaction.

2.6.2. TGA-DTG-DTA analysis

Thermogravimetric analysis (TGA/DTG/DTA) was performed using a Shimadzu DTG−60 Differential Thermal–Thermogravimetric Analyzer to evaluate the amount, thermal stability, and oxidation behavior of

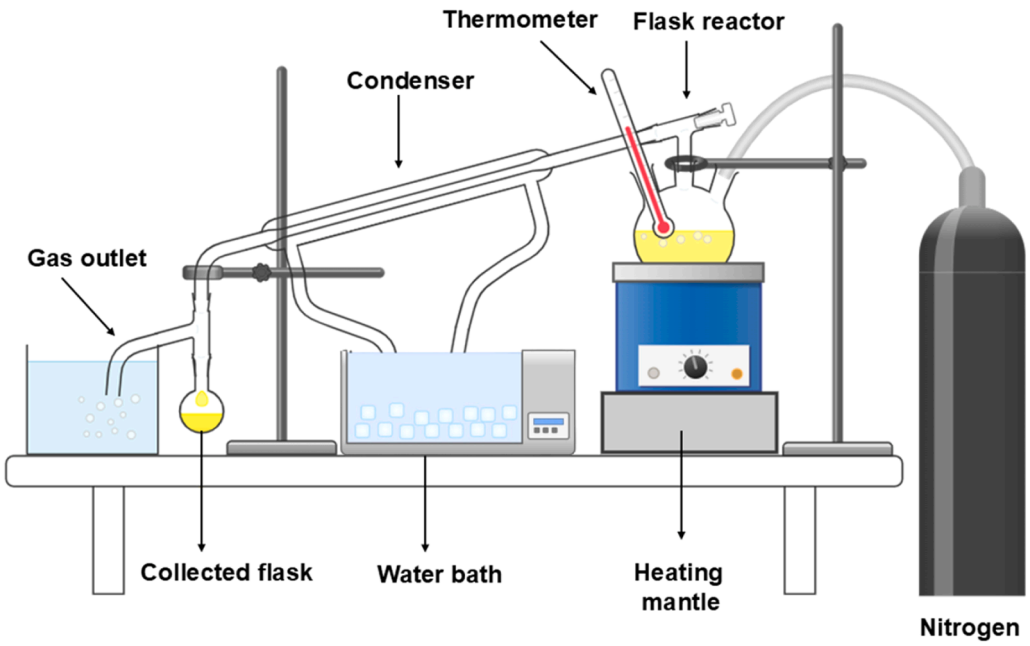

Fig. 1. Schematic diagram of the deoxygenation reaction.

carbonaceous deposits on the spent Ni–Mo/γ-Al_2O_3 catalyst. Prior to analysis, the spent catalyst was separated by filtration, washed repeatedly with n-hexane to remove residual reactants and soluble products, and dried in an oven. Approximately 10 mg of the dried sample was analyzed over a temperature range of 25–1100 °C. The instrument has a measurable TG range of ±500 mg, a DTA range of ±1000 μV, and a weight readability of 0.1 μg, and can operate under air or inert gas atmospheres.

2.7. Analysis of deoxygenation product

2.7.1. GC–MS analysis of hydrocarbon products

The liquid products obtained from the deoxygenation reaction were analyzed using gas chromatography–mass spectrometry (GC–MS) (Shimadzu QP−2010 SE) equipped with an Agilent DB−5MS UI capillary column (30 m × 0.25 mm i.d., 0.25 μm film thickness). Helium was used as the carrier gas. A 1 μL aliquot of the liquid product was injected in split mode at 300 °C with a split ratio of 54:1. The oven temperature program was identical to that used for feedstock analysis. The mass spectrometer operated in EI mode at 70 eV with a scan range of *m/z* 28–600. Compound identification was performed by comparing the obtained mass spectra with mass spectral libraries. The composition of the liquid products was determined by GC–MS and reported as relative hydrocarbon content (area%). This value was calculated by normalizing the sum of the hydrocarbon peak areas to the total peak area of all identified products according to Eq. (4). Selectivity for the desired hydrocarbon class was calculated as the percentage of the desired hydrocarbon peak area relative to the total hydrocarbon peak area according to Eq. (5).

$$\text{Relative hydrocarbon content(area\%)} = \left(\frac{\Sigma A_{hydrocarbon}}{\Sigma A_{total\ identified\ products}}\right) x100 \quad (4)$$

$$\text{Selevtivity(\%)} = \left(\frac{A_{desired\ hydrocarbon}}{\Sigma A_{hydrocarbon}}\right) x100 \quad (5)$$

2.7.2. ATR-FTIR analysis of liquid products

The chemical structure of the green diesel products was analyzed by ATR-FTIR (Shimadzu IRSpirit-T). Liquid samples were applied directly onto the ATR crystal, and spectra were recorded in the range of 4000–400 cm^{-1} . The spectra were processed and analyzed using Origin software to confirm the removal of oxygen-containing functional groups and the formation of hydrocarbon species.

2.8. Catalyst reproducibility, reusability, and stability test

The catalytic reproducibility, reusability, and stability of the Ni–Mo/γ-Al_2O_3 catalyst were evaluated to assess the reliability of the experimental results and the durability of the catalyst during repeated use. Catalytic reproducibility was first verified through four independent reactions using fresh catalyst under identical conditions, and the resulting liquid yields were compared to confirm consistent catalytic performance. Catalyst reusability was then investigated through consecutive reaction cycles using the same catalyst. After each cycle, the catalyst was recovered by filtration, washed with n-hexane to remove residual reactants and heavy products, and dried at 110 °C for 12 h before reuse under identical conditions. Catalytic stability was evaluated based on the variation in liquid yield across successive cycles. The spent Ni–Mo/γ-Al_2O_3 obtained after the reusability test was further analyzed by thermogravimetric analysis (TGA/DTG/DTA) to examine the carbonaceous deposits formed during the reaction.

3. Result and discussion

3.1. Impregnation followed by sonication of monometallic and bimetallic on γ-Al_2O_3 support

Fig. 2 presents a schematic illustration of the expected surface structure of γ-Al_2O_3-supported mono- and bimetallic catalysts after impregnation and sonication. During the impregnation step, metal precursor species (NiO and/or MoO_3) are assumed to interact with the hydroxylated surface of γ-Al_2O_3, which typically contains oxygen-containing surface functionalities, predominantly hydroxyl (–OH) groups. These surface hydroxyl groups act as anchoring sites for metal species through coordination interactions and electrostatic attraction, thereby facilitating the immobilization of metal precursors on the γ-Al_2O_3 surface [18,19] .

As schematically depicted in Fig. 2, the γ-Al_2O_3 framework is preserved as the structural backbone of the catalyst. The introduced metal

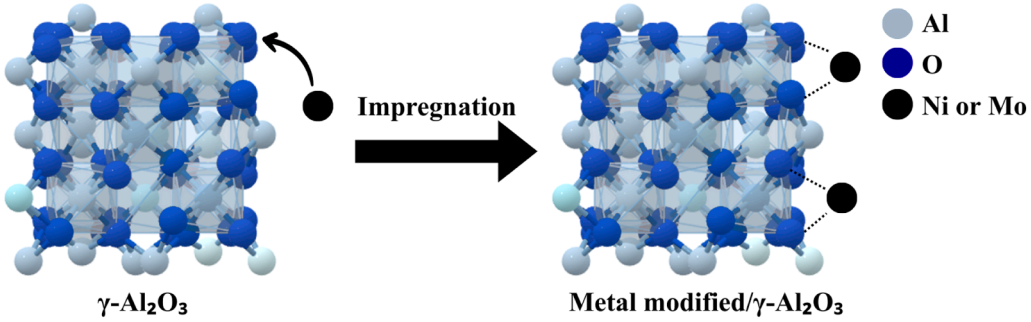

Fig. 2. Illustration of metal impregnation on γ-Al_2O_3 to form metal-modified γ-Al_2O_3 catalysts.

species are distributed on the external surface and within the pore structure as surface-associated entities. In this configuration, the metal species interact primarily with surface sites rather than substituting aluminum atoms within the γ-Al_2O_3 lattice. Therefore, the interaction can be described as a surface-level modification that alters the surface chemistry while preserving the structural integrity of the γ-Al_2O_3 support [21,60]. The subsequent sonication step enhances the homogeneity of metal distribution. Acoustic cavitation generated during sonication improves liquid penetration and surface wetting, thereby reducing localized precursor accumulation and promoting uniform dispersion of metal species [22]. This effect is particularly important for bimetallic systems, where close proximity between different metal species facilitates cooperative interactions while minimizing bulk phase segregation [23].

The Ni:Mo ratio plays an important role in determining the textural properties, active site distribution, and catalytic selectivity of Ni–Mo/γ-Al_2O_3 catalysts. Variations in this ratio can influence metal dispersion and metal–support interactions, thereby affecting pore accessibility and the availability of active sites. Previous studies on NiMo/γ-Al_2O_3 hydrotreating catalysts have employed Ni/Mo atomic ratios of 0.23–0.40 with total metal loadings of approximately 13–15 wt%, providing favorable metal dispersion and catalytic performance [24,25]. Excessive Mo loading may lead to the formation of MoO_x domains that partially occupy mesopores and reduce pore accessibility, whereas moderate Ni incorporation can enhance the dispersion of active sites on γ-Al_2O_3 [20]. The Ni:Mo ratio can also influence the preferred reaction pathways during deoxygenation. Ni-rich catalysts tend to favor decarboxylation and decarbonylation pathways, producing C_{15}–C_{17} hydrocarbons, whereas Mo-rich catalysts may promote hydrodeoxygenation routes leading to C_{16}–C_{18} hydrocarbons [20]. Balanced Ni–Mo ratios have been reported to promote synergistic interactions between Ni and Mo species, thereby improving catalytic activity and stability, which supports the selection of the 5 wt% Ni–5 wt% Mo composition used in this study [25]. Therefore, a 1:1 Ni:Mo ratio was selected in the present study to explore the cooperative roles of NiO and MoO_3 species under hydrogen-free deoxygenation conditions.

3.2. *Characteristics of metal modified γ-Al_2O_3 catalysts*

3.2.1. *Physical characteristics of catalysts*

The pristine γ-Al_2O_3 support (Fig. 3**a**) appears as a white powder, consistent with the high purity of transitional γ-Al_2O_3 and the absence of colored impurities. This observation agrees with the typical appearance of commercial γ-Al_2O_3 supports prior to metal impregnation [26]. After impregnation, the Ni/γ-Al_2O_3 catalyst (Fig. 3**b**) exhibits a greyish-green coloration. This color change is commonly reported for NiO-impregnated γ-Al_2O_3 catalysts and is consistent with the characteristic green color of nickel precursors and the formation of NiO-containing oxide species after calcination [27]. This observation provides qualitative evidence of the successful impregnation of NiO on the γ-Al_2O_3 surface.

The Mo/γ-Al_2O_3 catalyst (Fig. 3**c**) retains a pale white appearance, consistent with the color of ammonium heptamolybdate precursors. Such behavior is commonly reported for MoO_3-impregnated γ-Al_2O_3 catalysts, where Mo species are highly dispersed as molybdenum oxide or surface molybdate species that do not produce strong coloration at moderate metal loadings [28]. The bimetallic Ni–Mo/γ-Al_2O_3 catalyst (Fig. 3**d**) exhibits a light green coloration, intermediate between the Ni- and Mo-monometallic catalysts. This appearance reflects the combined presence of NiO and MoO_3 species on the γ-Al_2O_3 surface at lower individual metal loadings, as commonly observed for bimetallic catalysts prepared by impregnation. [9].

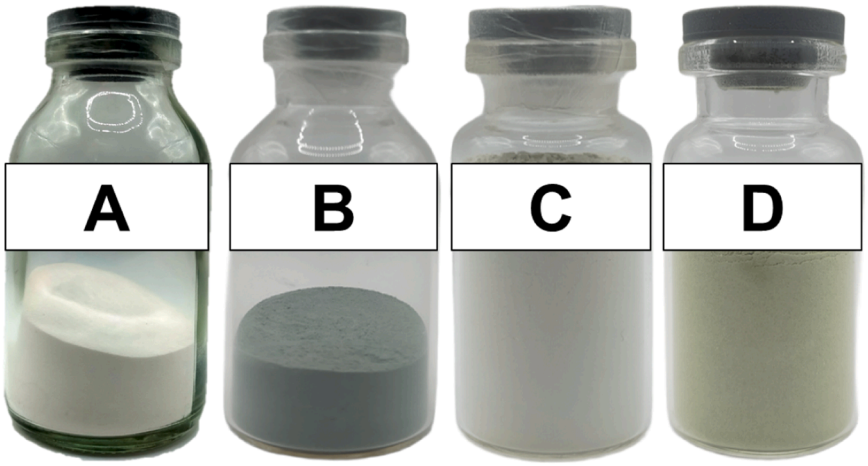

Fig. 3. Visual appearance of catalysts: (a) γ-Al_2O_3, (b) Ni/γ-Al_2O_3, (c) Mo/γ-Al_2O_3, and (d) Ni–Mo/γ-Al_2O_3.

3.2.2. Phase structure of metal-modified γ-Al₂O₃ by XRD

The X-ray diffraction patterns of γ-Al₂O₃ and the metal-modified catalysts are shown in Fig. 4**a**. The commercial γ-Al₂O₃ support exhibits reflections at 2θ ≈ 37.54°, 45.50°, and 67.12°, which correspond to the γ-Al₂O₃ phase and are commonly associated with its partially disordered structure and high specific surface area. [29]. For the Ni/γ-Al₂O₃ catalyst, diffraction peaks are observed at 2θ ≈ 37.22°, 43.36°, 45.55°, 62.93°, and 67.03°. The reflections at 43.36° and 62.93° closely match the standard NiO peaks (JCPDS 47–1049) at 43.30° and 62.90°, confirming the formation of crystalline NiO after calcination of $Ni(NO_3)_2{\cdot}6H_2O$. The peak at 37.22° overlaps with both NiO (37.26°) and γ-Al₂O₃ (37.54°), and its increased intensity relative to the bare support suggests a superposition of NiO and γ-Al₂O₃ reflections. Meanwhile, the γ-Al₂O₃ peaks at 45.55° and 67.03° remain clearly visible, indicating that the support structure is preserved after NiO incorporation. The appearance of distinct NiO reflections demonstrates that at 10 wt% loading, nickel species form detectable NiO crystallites. Similar behavior has been reported for Ni/γ-Al₂O₃ catalysts at moderate to high metal loadings, where metal–support interaction coexists with the partial formation of crystalline NiO domains [26].

In the Mo/γ-Al₂O₃ catalyst (10 wt% Mo), diffraction peaks appear at 2θ ≈ 20.84°, 22.05°, 23.48°, 25.50°, and 26.18°, together with γ-Al₂O₃ reflections at 45.65° and 67.33°. The reflections at 23.48° and 25.50° correspond well to the standard MoO₃ peaks (JCPDS 35–0609) at 23.30° and 25.72°. Meanwhile, the peaks at 20.84°, 22.05°, and 26.18° are close to those of $Al_2(MoO_4)_3$ (JCPDS 01–084–1652) at 20.90°, 22.22°, and 26.26°. These observations suggest that molybdenum species are present both as MoO₃-type oxide domains and as surface molybdate species formed through interactions between MoO_x and γ-Al₂O₃ during calcination. The γ-Al₂O₃ reflections at 45.65° and 67.33° remain visible, confirming that the γ-Al₂O₃ framework remains structurally intact. The formation of aluminum molybdate-like species through strong

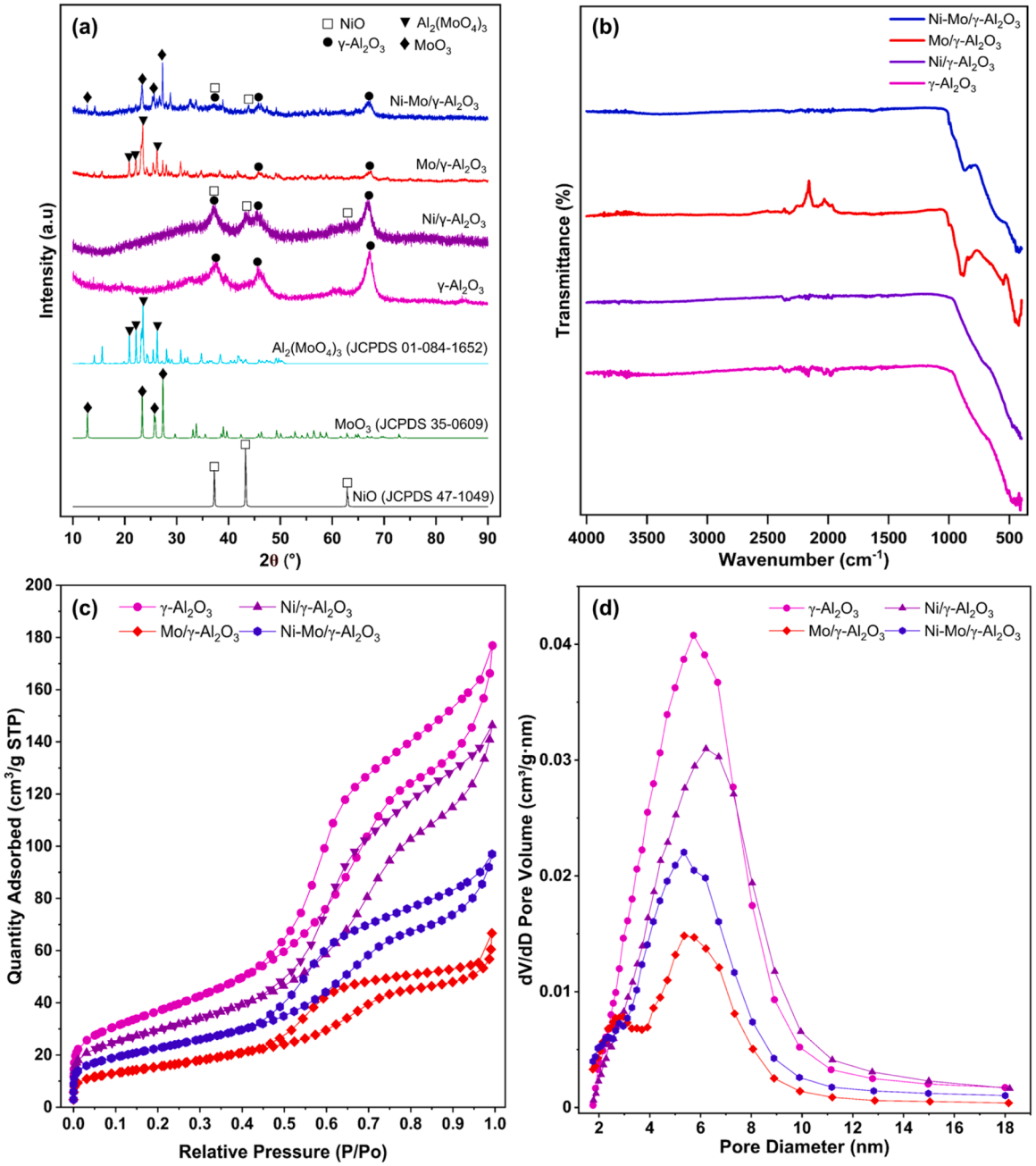

Fig. 4. XRD pattern of catalysts (a), ATR-FTIR spectra of catalysts (b), N_2 adsorption-desorption isotherms (c), and pore size distribution (d).

metal–support interactions has been widely reported for Mo/γ-Al_2O_3 systems [30].

For the bimetallic Ni–Mo/γ-Al_2O_3 catalyst (5 wt% Ni and 5 wt% Mo), diffraction peaks are observed at 2θ ≈ 12.76°, 23.26°, 25.63°, 27.29°, 37.13°, 43.80°, 45.78°, and 67.33°. The reflections at 12.76°, 23.26°, 25.63°, and 27.29° correspond to standard MoO_3 peaks (JCPDS 35–0609), indicating the presence of MoO_3 oxide domains. The reflections at 37.13° and 43.80° match NiO peaks (JCPDS 47–1049), confirming that NiO is also present in the bimetallic catalyst. Meanwhile, the γ-Al_2O_3 reflections at 45.78° and 67.33° remain visible, indicating that the support structure is preserved after co-impregnation. Notably, no diffraction peaks corresponding to metallic Ni or Ni–Mo alloy phases were detected. Because no pre-reduction treatment or external hydrogen was applied prior to the reaction, the catalyst remains in an oxidized state under hydrogen-free deoxygenation conditions. Therefore, the active phases in the Ni–Mo/γ-Al_2O_3 catalyst are identified as NiO and MoO_3 species supported on γ-Al_2O_3 [30].

3.2.3. *Surface chemical properties by ATR-FTIR*

The ATR-FTIR spectra of the γ-Al_2O_3 support and the metal-modified catalysts are presented in Fig. 4**b**. The pristine γ-Al_2O_3 exhibits absorption bands at approximately 514, 484, 446, 433, and 410 cm^{-1} , which are attributed to Al–O and Al–O–Al lattice vibrations characteristic of the γ-Al_2O_3 structure. These bands confirm that the γ-Al_2O_3 framework remains intact after thermal treatment [31]. For the Ni/γ-Al_2O_3 catalyst, absorption bands are observed at approximately 476, 446, 433, 422, and 409 cm^{-1} . Compared with the pristine support, slight shifts and variations in band intensity are evident, particularly in the 450–400 cm^{-1} region. In ATR-FTIR measurements, such changes indicate perturbations in Al–O vibrations resulting from interactions between NiO species and the γ-Al_2O_3 surface. The absence of distinct new bands at higher wavenumbers suggests that NiO species remain highly dispersed on the γ-Al_2O_3 surface rather than forming bulk NiO phases, consistent with the XRD results [32].

The ATR-FTIR spectrum of the Mo/γ-Al_2O_3 catalyst shows pronounced spectral modifications. New absorption bands appear at approximately 999, 901, 878, and 837 cm^{-1} . The band near 999 cm^{-1} is commonly attributed to the stretching vibration of terminal Mo═O species, while bands in the 900–800 cm^{-1} region correspond to bridging Mo–O–Mo or Mo–O–Al vibrations. These features indicate the presence of surface molybdenum oxide or molybdate-type species interacting strongly with γ-Al_2O_3. Additional bands observed at around 549, 450, and 425 cm^{-1} are associated with lattice vibrations involving Mo–O and Al–O bonds, further supporting strong Mo–support interactions. These observations are consistent with the partial formation of aluminum molybdate phases inferred from the XRD analysis at higher Mo loading [30,32] .

For the bimetallic Ni–Mo/γ-Al_2O_3 catalyst, absorption bands are detected at approximately 996, 875, 818, 444, and 420 cm^{-1} . The persistence of bands in the 1000–800 cm^{-1} region confirms the presence of Mo oxide species on the catalyst surface. Compared with the monometallic Mo/γ-Al_2O_3 catalyst, the slight shift of these bands toward lower wavenumbers and their reduced number suggest a modified local coordination environment of MoO_3 species due to the coexistence of NiO. Meanwhile, the Al–O lattice vibration bands remain largely unchanged, indicating that the γ-Al_2O_3 framework is preserved and that impregnation mainly affects surface chemistry rather than the bulk structure [27, 28] .

3.2.4. *Textural properties and porous structure of metal-modified γ-Al_2O_3 derived from N_2 adsorption–desorption*

As presented in Fig. 4**c**, the N_2 adsorption–desorption isotherms of γ-Al_2O_3 and all metal-modified catalysts exhibit classical type IV behavior according to the IUPAC classification, confirming the predominance of mesoporous structures. The corresponding hysteresis loops are identified as H2 type, indicating a disordered mesoporous network governed by pore blocking and percolation effects typical of γ-Al_2O_3-derived materials. This behavior is consistent with the structural characteristics of transition γ-Al_2O_3, which commonly exhibits ink-bottle–type mesopores formed by aggregated crystalline domains [33].

According to Table 2, pristine γ-Al_2O_3 exhibits the highest specific surface area of 133.20 m^2 g^{-1} and the largest mesopore volume of 0.278 cm^3 g^{-1} . As shown in Fig. 4**c**, this is reflected by the highest nitrogen uptake along the adsorption branch. The pore size distribution in Fig. 4**d** displays a sharp and intense peak in the mesoporous region, with an average pore diameter of 7.29 nm as listed in Table 2. The high differential pore volume intensity indicates a well-developed mesoporous network, which is favorable for the diffusion of bulky triglyceride and long-chain fatty acid molecules during catalytic upgrading processes [34].

After NiO incorporation, the structural parameters decrease moderately. As shown in Table 2, the specific surface area decreases from 133.20 to 106.62 m^2 g^{-1} , while the mesopore volume decreases from 0.278 to 0.230 cm^3 g^{-1} . In Fig. 4**c**, nitrogen uptake is slightly lower than that of γ-Al_2O_3, although the type IV–H2 isotherm profile is preserved, indicating that the mesoporous framework remains structurally intact. The pore size distribution in Fig. 4**d** shows a slight decrease in intensity, accompanied by an increase in the average pore diameter to 7.71 nm as listed in Table 2. This behavior suggests partial occupation of smaller mesopores and redistribution toward relatively larger accessible channels. Such moderate textural modification indicates good dispersion of NiO species without significant pore collapse, consistent with the reported behavior of mesoporous NiO-supported catalysts in deoxygenation systems [32].

Mo loading induces a significant deterioration of textural properties. As shown in Table 2, the specific surface area decreases drastically to 56.44 m^2 g^{-1} and the mesopore volume to 0.103 cm^3 g^{-1} , representing substantial reductions relative to the parent γ-Al_2O_3 support. This decline is clearly reflected in Fig. 4**c,** where the total nitrogen uptake is markedly reduced. The pore size distribution in Fig. 4**d** exhibits a pronounced decrease in peak intensity, while the average pore diameter slightly decreases to 6.98 nm. These results indicate that MoO_x species partially occupy and block internal mesoporous channels rather than depositing solely on the external surface. Such aggregation behavior of MoO_x on γ-Al_2O_3 has been widely reported and can reduce structural accessibility despite the intrinsic activity of Mo species for C–O bond cleavage [28].

The bimetallic Ni–Mo/γ-Al_2O_3 catalyst exhibits intermediate textural characteristics between the NiO- and MoO_3-loaded samples. As shown in Table 2, the specific surface area is 81.36 m^2 g^{-1} and the mesopore volume is 0.150 cm^3 g^{-1} , indicating moderate reductions compared with the parent γ-Al_2O_3 support. In Fig. 4**c**, the nitrogen uptake is higher than that of Mo/γ-Al_2O_3 but lower than that of Ni/γ-Al_2O_3, suggesting partial preservation of porosity. The pore size distribution in Fig. 4**d** confirms a mesoporous structure with an average pore diameter of 7.03 nm. Importantly, the pore distribution intensity is significantly higher than that observed for Mo/γ-Al_2O_3, indicating that NiO incorporation mitigates excessive MoO_3 aggregation and promotes improved dispersion within the γ-Al_2O_3 framework. Such structural moderation

Table 2
Physicochemical properties of catalysts.

Catalyst	Surface area (m^2/g)			Pore volume (cm^3/g)	Pore diameter (nm)
	S_{BET}	S_{meso}	S_{ext}	V_{meso}	Mesoporous
γ-Al_2O_3	133.2	152.91	133.73	0.278	7.29
Ni/γ-Al_2O_3	106.62	119.48	105.04	0.23	7.71
Mo/γ-Al_2O_3	56.44	58.92	56.9	0.103	6.98
Ni–Mo/γ-Al_2O_3	81.36	84.86	79.35	0.15	7.03

supports the synergistic interaction between NiO and MoO_3 species, as widely reported for γ-Al_2O_3-supported bimetallic deoxygenation catalysts [30].

3.2.5. *Morphology and elemental distribution of catalysts revealed by SEM–EDX mapping*

SEM images recorded at 500 × magnification reveal clear morphological and compositional evolution after metal incorporation onto γ-Al_2O_3. As shown in Fig. 5**a**, pristine γ-Al_2O_3 consists of irregular agglomerated particles with fractured and rough surfaces, typical of mesoporous γ-Al_2O_3 formed through particle aggregation. The particle size distribution is relatively broad, with an average diameter of 62.70 μm, indicating notable agglomeration. EDX spectra and elemental mapping confirm a homogeneous distribution of Al (51.7%) and O (48.3%), demonstrating the structural purity and compositional uniformity of the support. Similar SEM–EDX characteristics of γ-Al_2O_3 supports, including rough aggregated particles and uniform Al–O distribution, have been widely reported in hydroprocessing and deoxygenation studies, highlighting the role of surface roughness in facilitating metal anchoring and dispersion. [20,21,35].

As shown in Fig. 5**b**, the Ni/γ-Al_2O_3 catalyst exhibits a noticeable reduction in particle size after Ni impregnation, with the average diameter decreasing to 22.49 μm, accompanied by a more compact and granular surface texture. This morphological refinement suggests partial fragmentation and restructuring of γ-Al_2O_3 aggregates induced by metal–support interactions during impregnation and calcination. EDX analysis confirms the presence of Ni (30.44%), while elemental mapping reveals a relatively uniform distribution of Ni across the γ-Al_2O_3 surface with localized enrichment regions. Similar SEM–EDX observations have been reported for Ni/γ-Al_2O_3 catalysts, where NiO nanoparticles form surface clusters that increase the density of accessible redox-active sites while remaining well anchored to the γ-Al_2O_3 matrix [17].

Mo/γ-Al_2O_3 catalyst in Fig. 5**c** displays moderately sized aggregates with an average particle diameter of 29.47 μm, larger than Ni/γ-Al_2O_3 but significantly smaller than pristine γ-Al_2O_3. The surface appears smoother and more uniformly coated, indicating the formation of finely dispersed MoO_x species. EDX mapping reveals a homogeneous distribution of Mo (29.15%), Al (33.29%), and O (37.56%). SEM–EDX studies reported in the literature consistently show that MoO_x species preferentially anchor onto γ-Al_2O_3 in a highly dispersed or partially amorphous form, which often explains their weak or undetectable diffraction signals in XRD despite strong catalytic activity in deoxygenation reactions [20].

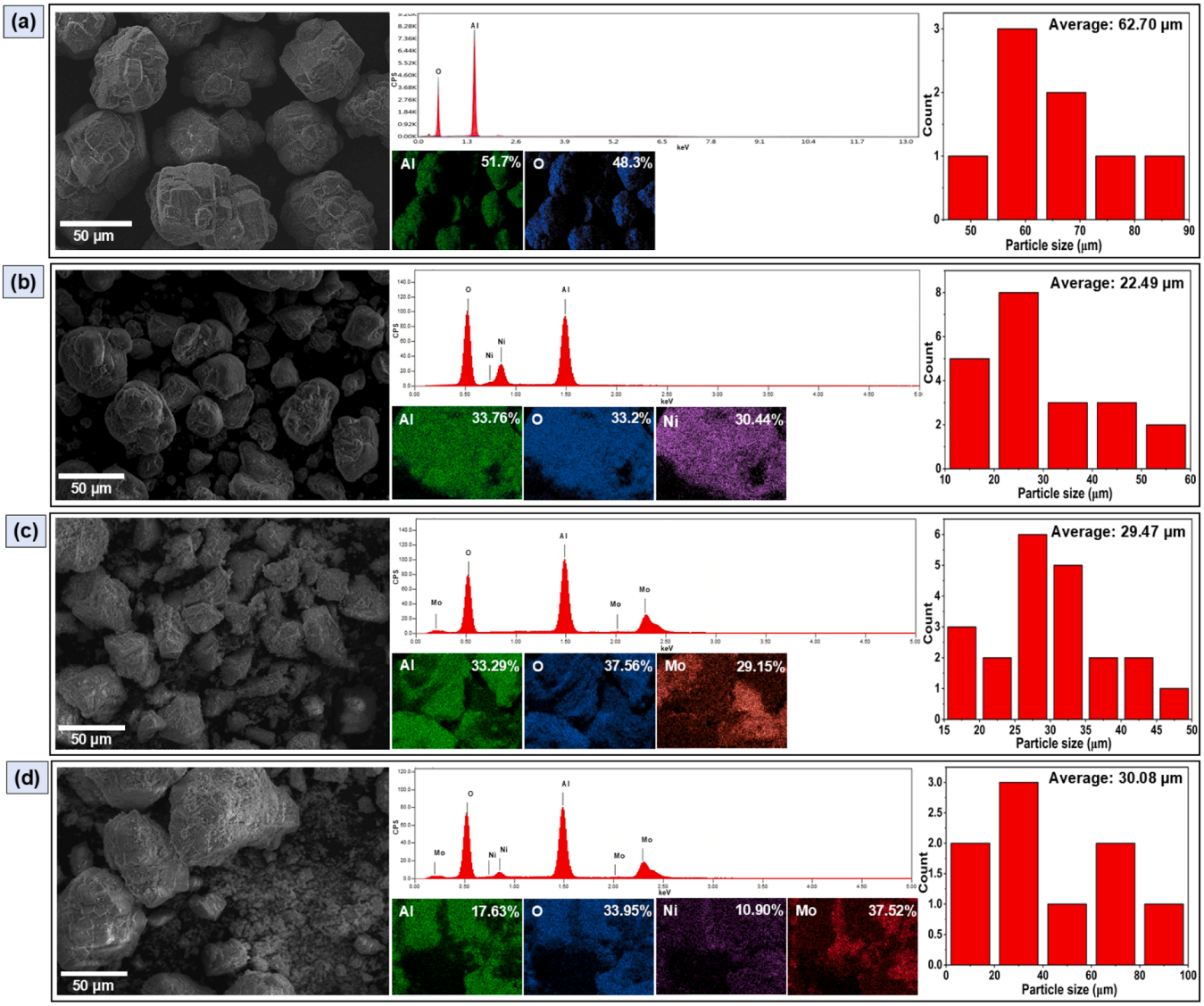

Fig. 5. SEM–EDX analysis of the catalysts, showing surface morphology at 500 × magnification, corresponding EDX spectra, elemental mapping images, elemental distribution, and particle size distribution for (a) γ-Al_2O_3, (b) Ni/γ-Al_2O_3, (c) Mo/γ-Al_2O_3, and (d) Ni–Mo/γ-Al_2O_3.

The Ni–Mo/γ-Al_2O_3 catalyst (Fig. 5**d**) exhibits a well-integrated morphology characterized by densely packed aggregates and an intermediate average particle size of 30.08 μm. Although the particle size distribution is broader than that of Ni/γ-Al_2O_3, the surface texture appears more homogeneous, suggesting cooperative restructuring induced by bimetallic interactions. EDX spectra confirm the coexistence of Ni (10.90%) and Mo (37.52%), while elemental mapping reveals clear spatial overlap between the two metals, indicating close interfacial contact. Previous SEM–EDX studies of Ni–Mo/γ-Al_2O_3 catalysts have shown that such co-localization of NiO and MoO_3 is an important prerequisite for bimetallic synergy, facilitating enhanced oxygen removal through complementary redox pathways and improving catalytic stability during deoxygenation reactions [17].

The relatively uniform distribution of Ni and Mo species observed in the SEM–EDX mapping indicates that the ultrasonic treatment applied after the impregnation step contributed to improved dispersion of metal precursors on the γ-Al_2O_3 support. Ultrasonic irradiation generates acoustic cavitation in the liquid phase, producing localized shear forces and microjets that enhance mass transfer and promote the penetration of metal precursor species into the pore structure of the support. Previous studies have reported that ultrasound-assisted impregnation can reduce particle aggregation, improve metal dispersion, and better preserve the textural properties of supported catalysts compared with conventional wet impregnation methods. In particular, ultrasonic treatment has been shown to minimize pore blockage and promote a more homogeneous distribution of active metal species on porous supports [18,19,36].

3.2.6. *Metal loading analysis by ICP-OES*

The actual metal loadings of the prepared catalysts were determined by inductively coupled plasma optical emission spectroscopy (ICP-OES), and the results are summarized in Table 3. The Ni content in the Ni/γ-Al_2O_3 catalyst was measured to be 9.87%, while the Mo/γ-Al_2O_3 catalyst exhibited a Mo content of 9.92%, both of which are close to the nominal loading of 10%. For the bimetallic Ni–Mo/γ-Al_2O_3 catalyst, the measured Ni and Mo contents were 4.89% and 4.96%, respectively, which agree well with the targeted loading of 5% for each metal. The slight deviations from the nominal values may be attributed to minor losses during the impregnation, drying, and calcination steps. Overall, the ICP-OES results confirm that the desired metal compositions were successfully achieved in all synthesized catalysts [20].

3.3. *Metal modified γ-Al_2O_3 as catalyst for deoxygenation of waste corn oil*

Washing is a crucial pretreatment step to remove polar impurities such as water, salts, phospholipids, and oxidation by-products that can poison active sites and promote coke formation during deoxygenation [33,37]. The waste corn oil was washed with hot water at approximately 70–80 °C, followed by phase separation, which effectively reduces polar and inorganic contaminants without altering the fatty acid backbone [38]. Previous studies have shown that such simple water-washing or degumming pretreatments improve catalyst stability, enhance liquid hydrocarbon yield, and suppress coke formation in deoxygenation of vegetable oils [39]. By minimizing the presence of polar species that favor condensation reactions, feedstock washing contributes to more consistent catalytic performance and improved selectivity toward green diesel-range hydrocarbons [39].

The liquid products obtained from the deoxygenation reactions exhibit distinct colour differences depending on the catalyst used, as shown in Fig. 6. The product derived from γ-Al_2O_3 appears light yellow, the Ni/γ-Al_2O_3 product shows a slightly darker yellow colour, the Mo/γ-Al_2O_3 product remains relatively pale, whereas the Ni–Mo/γ-Al_2O_3 catalyst produces the darkest amber-coloured liquid. In hydrogen-free deoxygenation systems, product colour is commonly associated with the extent of conversion, the persistence of oxygenated compounds, and the formation of heavier hydrocarbons or condensed aromatic species generated through secondary condensation and cyclization reactions [17,40]. Accordingly, the darker colour observed for the Ni–Mo-derived product suggests a higher degree of deoxygenation and hydrocarbon formation. In contrast, the paler product obtained over Mo/γ-Al_2O_3 indicates a lower conversion extent or a higher fraction of residual oxygenated species, consistent with observations reported in previous deoxygenation studies of vegetable oils and fatty acids. This visual observation is consistent with the GC–MS analysis discussed in the following section [34,36].

Quantitative product distributions presented in Fig. 7 further supports these observations. The bimetallic Ni–Mo/γ-Al_2O_3 catalyst achieves the highest liquid yield of 39.66% together with the lowest coke yield of 33.70%. In comparison, Mo/γ-Al_2O_3 produces a liquid yield of 35.29% with a significantly higher coke yield of 39.33%, while Ni/γ-Al_2O_3 and the bare γ-Al_2O_3 support yield lower liquid fractions of approximately 32–33%. The highest coke formation is observed for γ-Al_2O_3 at 41.80%. Gas yields remain relatively constant for all catalysts in the range of 25–28%, indicating that the primary differences among catalysts arise from the competition between liquid hydrocarbon formation and coke generation rather than gas production. The superior liquid yield obtained over Ni–Mo/γ-Al_2O_3 is attributed to cooperative structural and bifunctional effects. XRD analysis confirms the presence of NiO and MoO_3 without alloy formation, while N_2 adsorption–desorption results indicate preserved mesoporosity that maintains accessibility for bulky triglyceride molecules. SEM–EDX mapping further reveals homogeneous dispersion and spatial proximity of Ni and Mo species, enabling cooperative C–O bond cleavage and stabilization of reaction intermediates. The simultaneous increase in liquid yield and decrease in coke formation therefore demonstrate a clear structure–performance relationship governed by balanced active sites and preserved mesoporous channels. [34,36].

These trends can be rationalized by considering the dominant hydrogen-free deoxygenation pathways, namely decarboxylation (DCO_2) and decarbonylation (DCO). Ni-based catalysts are widely reported to promote these reactions for long-chain fatty acids, producing hydrocarbons with one carbon atom fewer than the parent fatty acid together with the release of CO and CO_2. Under hydrogen-free conditions, Ni/γ-Al_2O_3 catalysts may also facilitate secondary cracking and condensation reactions of reactive intermediates, which can increase gas formation and coke deposition. Such behavior has been reported for Ni/γ-Al_2O_3 catalysts operating under inert atmospheres, where moderate liquid yields are often accompanied by relatively high gas and coke fractions [40,41]

For Mo/γ-Al_2O_3, although Mo-based catalysts are capable of promoting deoxygenation via DCO and DCO_2 pathways, their catalytic performance is highly dependent on metal dispersion and pore accessibility. Structural characterization in this study indicates that high Mo loading leads to the formation of Mo-rich domains and partial aluminum molybdate, which causes pore blockage and reduced accessibility of active sites. Similar observations reported in the literature show that aggregated Mo species and molybdate formation on γ-Al_2O_3 can promote polymerization and condensation of oxygenated intermediates, thereby increasing coke formation and limiting the relative hydrocarbon yield in deoxygenation reactions. [28,42].

The enhanced liquid yield over Ni–Mo/γ-Al_2O_3 is attributed to cooperative structural and bifunctional effects under hydrogen-free deoxygenation conditions. XRD analysis confirms the presence of NiO and MoO_3 phases without detectable alloy formation, indicating that the

Table 3
Metal loading of catalysts determined by ICP-OES.

Catalyst	Ni (%)	Mo (%)
Ni/γ-Al_2O_3	9.87	-
Mo/γ-Al_2O_3	-	9.92
Ni–Mo/γ-Al_2O_3	4.89	4.96

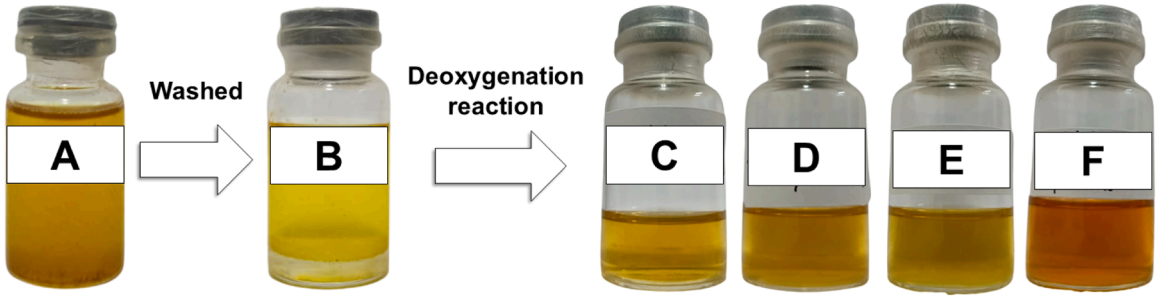

Fig. 6. Visual appearance of green diesel products using different catalysts: (a) waste corn oil, (b) washed corn oil, (c) γ-Al_2O_3, (d) Ni/γ-Al_2O_3, (e) Mo/γ-Al_2O_3, and (f) Ni–Mo/γ-Al_2O_3.

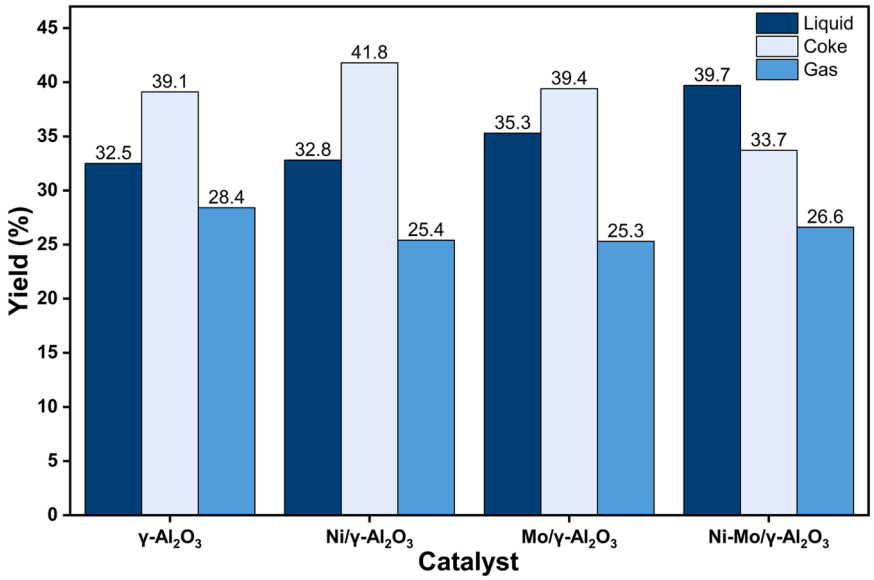

Fig. 7. Yield of liquid product, coke, and gas.

catalytic behavior originates from oxide species rather than metallic Ni–Mo interactions. N_2 adsorption–desorption analysis demonstrates preserved mesoporosity sufficient to accommodate bulky triglyceride molecules, while SEM–EDX mapping reveals relatively homogeneous dispersion and close spatial proximity of Ni and Mo species on the γ-Al_2O_3 support. This interfacial proximity enables cooperative catalysis: NiO promotes C–O bond cleavage through DCO and DCO_2 pathways, whereas MoO_3 moderates the reactivity of oxygenated intermediates and suppresses excessive condensation reactions that lead to coke formation. Consequently, the simultaneous increase in liquid yield and decrease in coke formation demonstrate a clear structure–performance relationship governed by balanced active sites, preserved mesoporosity, and synergistic Ni–Mo functionality. Similar cooperative behavior has been widely reported for Ni–Mo/γ-Al_2O_3 catalysts in hydrogen-free or low-hydrogen deoxygenation systems, where bimetallic formulations consistently outperform their monometallic counterparts in terms of liquid yield and coke resistance [17,43].

3.4. Characterization of coke deposit from deoxygenation of waste corn oil

3.4.1. ATR-FTIR analysis

Fig. 8 presents the ATR-FTIR spectra of γ-Al_2O_3, Ni/γ-Al_2O_3, Mo/γ-Al_2O_3, and Ni–Mo/γ-Al_2O_3 catalysts after the deoxygenation of waste corn oil. In such systems, reduced transmittance generally indicates the accumulation of carbonaceous deposits formed through secondary condensation, cyclization, and polymerization of oxygenated

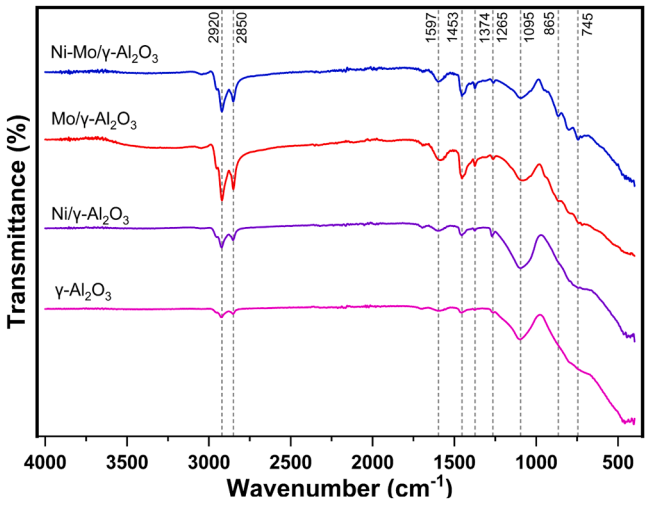

Fig. 8. ATR-FTIR spectra of coke deoxygenation reaction.

intermediates during the reaction [41,44]. The γ-Al_2O_3 support exhibits the highest transmittance with negligible absorption at 2920 and 2850 cm^{-1}, indicating minimal aliphatic hydrocarbon deposition. These bands correspond to the asymmetric and symmetric stretching vibrations of aliphatic –CH_2– groups commonly observed in hydrocarbon

residues formed during fatty acid conversion [45]. The weak signals near 1597 cm^{-1} and 1453–1374 cm^{-1} indicate very limited aromatic C═C and CH bending vibrations, confirming negligible coke formation. Bands below 1000 cm^{-1} are mainly attributed to γ-Al_2O_3 lattice vibrations rather than organic residues [46].

The Ni/γ-Al_2O_3 catalyst shows moderate absorption bands at 2920 and 2850 cm^{-1}, confirming the formation of aliphatic hydrocarbons through decarboxylation and decarbonylation pathways. The bands at 1453 and 1374 cm^{-1} correspond to CH_2 scissoring and CH_3 bending vibrations, indicating the presence of alkyl-rich deposits [40]. Under hydrogen-free deoxygenation conditions, Ni surfaces promote DCO and DCO_2 reactions but may also facilitate secondary cracking and condensation of reactive intermediates, leading to partial coke accumulation. The relatively weak C–O stretching vibrations at 1265 and 1095 cm^{-1} indicate limited persistence of oxygenated species [35,47].

The Mo/γ-Al_2O_3 catalyst exhibits stronger absorption bands at 1265 and 1095 cm^{-1}, corresponding to C–O stretching vibrations of phenolic-, ether-, or ester-type species [46,48]. This observation indicates incomplete conversion of oxygenates and the accumulation of oxygen-containing intermediates on the catalyst surface. The band at approximately 1597 cm^{-1}, attributed to aromatic C═C stretching vibrations, suggests the formation of conjugated structures that act as precursors to polyaromatic coke during biomass oil deoxygenation. Similar behavior has been reported for Mo-based catalysts, where insufficient hydrogen transfer promotes polymerization of reactive oxygenated intermediates [48].

The Ni–Mo/γ-Al_2O_3 catalyst exhibits the lowest transmittance over most spectral regions, indicating the highest surface accumulation of carbonaceous species. Strong absorption bands at 2920 and 2850 cm^{-1} confirm significant aliphatic hydrocarbon deposition, while the distinct bands at 1597, 865, and 745 cm^{-1} correspond to aromatic and polyaromatic C–H out-of-plane bending vibrations [36,40,44]. These spectral features are commonly associated with more condensed coke structures formed during prolonged deoxygenation reactions. However, the comparatively weaker C–O bands compared with Mo/γ-Al_2O_3 indicate more complete conversion of oxygenated intermediates. Similar synergistic effects in Ni–Mo systems, where NiO enhances DCO activity while MoO_3 stabilizes reaction intermediates and limits excessive oxygen retention, have been reported in vegetable oil deoxygenation studies [28,44].

3.4.2. TGA-DTG-DTA analysis

Thermogravimetric analysis (TGA) coupled with DTG and DTA (Fig. 9) was conducted to quantify coke deposition on the spent Ni–Mo/γ-Al_2O_3 catalyst after the deoxygenation reaction. Prior to analysis, the spent catalyst was separated by filtration, washed several times with n-hexane to remove residual reactants, and dried in an oven at 110 °C for 12 h. Thus, the observed mass loss mainly corresponds to carbonaceous deposits strongly bound to the catalyst surface, which are considered a major cause of catalyst deactivation during repeated catalytic cycles [9].

The TG profile shows a total mass loss of approximately 11.8 wt%, attributed to the oxidation of carbon deposits formed during the reaction. Two distinct oxidation regions are observed in the DTG profile. The first region at 300–400 °C corresponds to the oxidation of soft coke (~3.8 wt%), which generally consists of less-condensed carbon species derived from partially polymerized intermediates. The second region at 400–600 °C corresponds to the oxidation of hard coke (~7.2 wt%), associated with more condensed and thermally stable carbon structures. The DTA curve exhibits a strong exothermic peak centered at ~500 °C, confirming the oxidative combustion of these carbon deposits [9,32,49]. The predominance of high-temperature oxidation indicates that a significant fraction of the deposited carbon consists of thermally stable coke species capable of blocking active sites and contributing to catalyst deactivation. Similar coke deposition behavior has been reported for Ni–Mo-based catalysts in fatty acid upgrading and hydrodeoxygenation reactions [25,49].

3.5. Characterization of feedstocks and liquid products from deoxygenation of waste corn oil

3.5.1. GC-MS characterization

The chromatograms shown in Fig. 10 reveal a pronounced shift in product distribution after catalytic deoxygenation compared with the waste corn oil feedstock. The feedstock chromatogram in Fig. 10**a** displays dominant peaks within the retention time range of 24.896–37.738 min, which are characteristic of intact triglycerides and long-chain fatty acid esters commonly present in vegetable oils [46,50]. Such high retention times correspond to high-boiling oxygenated compounds. The detailed GC–MS analysis of the waste corn oil feedstock, including the identified fatty acids, their retention times, and relative peak area distributions, is summarized in Table S1. After treatment over γ-Al_2O_3, the chromatogram in Fig. 10**b** extends over the retention time range of 2.522–22.595 min, indicating partial cracking and ester decomposition but the persistence of oxygenated intermediates. Similar behavior has been reported for γ-Al_2O_3-supported systems lacking strong metallic functionality, where incomplete deoxygenation results in

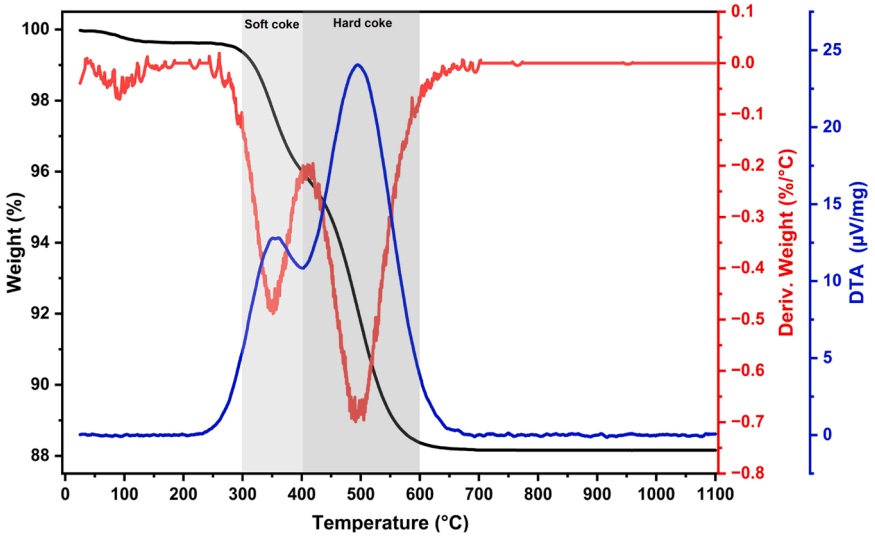

Fig. 9. TGA/DTG/DTA of spent catalyst Ni–Mo/γ-Al_2O_3.

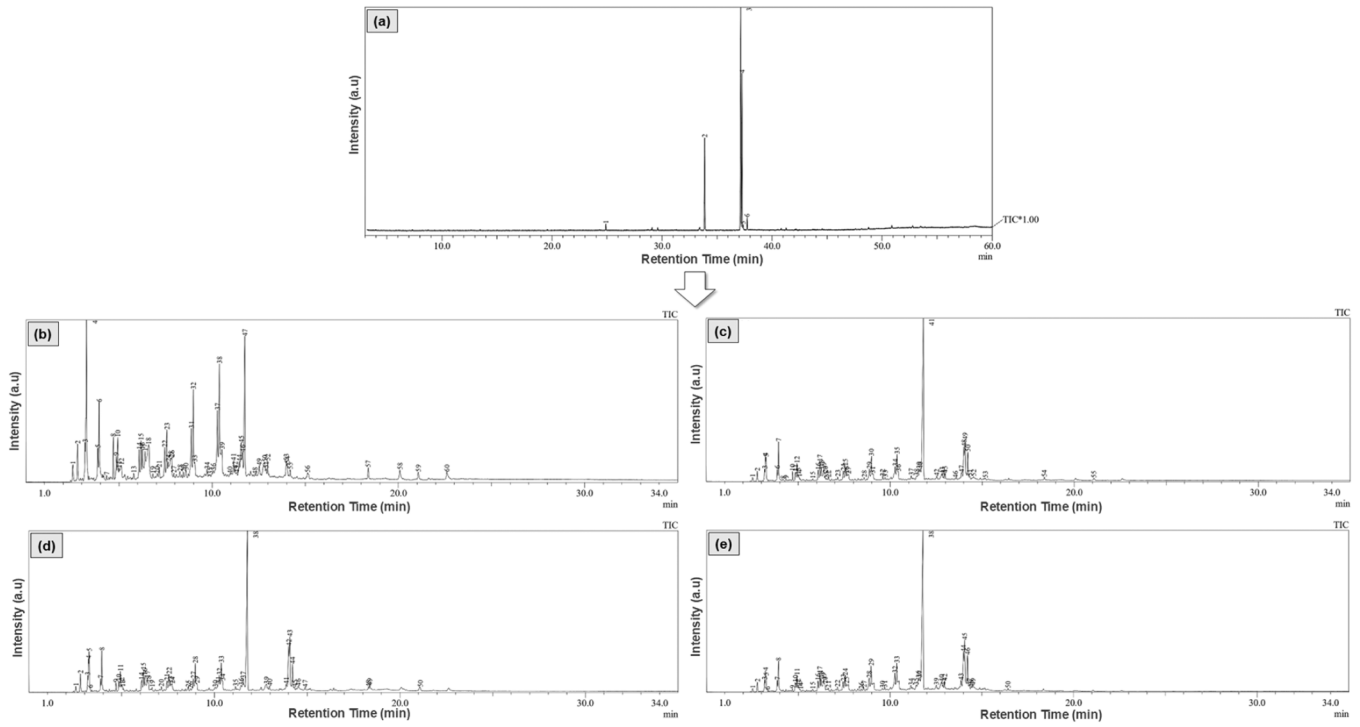

Fig. 10. Gas chromatograms of waste corn oil feedstock and liquid products obtained after deoxygenation over different catalysts: (a) waste corn oil, (b) γ-Al_2O_3, (c) Ni/γ-Al_2O_3, (d) Mo/γ-Al_2O_3, and (e) Ni–Mo/γ-Al_2O_3.

mixtures of oxygenates and hydrocarbons [46]. The detailed GC–MS characterization of the liquid products obtained from the deoxygenation of waste corn oil over the γ-Al_2O_3 catalyst, including compound identification, retention times, and relative peak area distributions, is summarized in Table S2.

The Ni/γ-Al_2O_3 product shown in Fig. 10**c** extends over the retention time range of 2.521–21.063 min and exhibits a pronounced increase in early-to-mid retention-time peaks associated with hydrocarbon formation. Ni-based catalysts are widely recognized to promote decarboxylation and decarbonylation of long-chain fatty acids, generating Cn−1 hydrocarbons accompanied by the release of CO and CO_2 [4,5]. Under hydrogen-free conditions, Ni surfaces may also catalyze secondary cracking reactions, producing lighter hydrocarbon fragments and increasing gas formation, consistent with the higher gas and coke tendency observed experimentally [40,47]. A comprehensive summary of the GC–MS analysis of the liquid products generated from the deoxygenation of waste corn oil over the Ni/γ-Al_2O_3 catalyst, comprising compound identification together with their respective retention times and relative peak area percentages, is provided in Table S3.

For the Mo/γ-Al_2O_3 catalyst shown in Fig. 10**d**, the retention time range remains 2.526–21.086 min, but relatively stronger mid-to-high retention time peaks persist, indicating incomplete removal of oxygenated intermediates. Mo-based catalysts are known to exhibit catalytic performance strongly dependent on metal dispersion and site accessibility; aggregated MoOx species may limit complete conversion and favor the accumulation of partially deoxygenated compounds. This behavior explains the higher coke yield and moderate liquid yield observed for this catalyst [28,43]. The GC–MS results of the liquid products obtained from the deoxygenation of waste corn oil over the Mo/γ-Al_2O_3 catalyst, including compound identification, retention times, and relative peak area percentages, are summarized in Table S4.

The Ni–Mo/γ-Al_2O_3 chromatogram in Fig. 10**e** is concentrated within a narrower retention time range of 2.518–16.432 min, showing almost complete suppression of high-retention-time ester peaks and a dominant hydrocarbon signature in the mid-retention-time region characteristic of diesel-range alkanes. The shift of the chromatographic distribution toward lower retention times indicates more effective deoxygenation and improved selectivity toward mid-chain hydrocarbons. Similar chromatographic shifts toward shorter retention times have been reported for Ni–Mo/γ-Al_2O_3 catalysts exhibiting strong bimetallic synergy in vegetable oil deoxygenation systems. This observation is consistent with the superior liquid yield and reduced coke formation observed for the Ni–Mo/γ-Al_2O_3 catalyst [38,44]. The compositional profile of the liquid products derived from the deoxygenation of waste corn oil over the Ni–Mo/γ-Al_2O_3 catalyst, including compound identification together with their respective retention times and relative peak area contributions, is systematically summarized in Table S5.

3.5.2. *Feedstock composition of waste corn oil*

Table S1 presents the derived free fatty acid distribution of the waste corn oil feedstock used in this study. The composition includes lauric acid (C12:0) at 1.28%, palmitic acid (C16:0) at 17.45%, linoleic acid (C18:2) at 46.38%, oleic acid (C18:1) at 32.45% (calculated as the sum of two peaks), and stearic acid (C18:0) at 2.43%. The GC–MS analysis summarized in Fig. 10**a** and Table S1 demonstrates that the waste corn oil feedstock is dominated by long-chain C18 fatty acids, particularly linoleic and oleic acids, while palmitic acid contributes a moderate fraction and shorter-chain acids remain minor components. Such a composition is consistent with typical corn oil profiles reported in the literature, where unsaturated C18 fatty acids constitute the majority of the lipid fraction [28,50].

The predominance of C18 fatty acids has direct implications for product distribution under deoxygenation conditions. In hydrogen-free systems, decarboxylation and decarbonylation pathways convert C18 fatty acids primarily into C17 hydrocarbons through the removal of CO_2 or CO, respectively, while palmitic acid (C16:0) favors the formation of C15 hydrocarbons via analogous deoxygenation pathways [40,47]. As a result, the intrinsic feed composition promotes the formation of hydrocarbons within the C15–C17 range, corresponding to diesel-range fractions. Similar carbon-number shifts from C18 fatty acids to C17 hydrocarbons have been documented in the catalytic deoxygenation of vegetable oils and fatty acids over Ni- and Ni–Mo-based catalysts. The

predominance of unsaturated C18 fatty acids is particularly advantageous for catalytic upgrading, since decarboxylation and decarbonylation of C18 species produce hydrocarbons within the C15–C18 window, which corresponds to the typical boiling range of green diesel fuels [28,44].

3.5.3. Liquid composition of deoxygenation products

Fig. 11**a** presents the detailed composition of liquid products obtained from the deoxygenation of washed waste corn oil over γ-Al_2O_3, Ni/γ-Al_2O_3, Mo/γ-Al_2O_3, and Ni–Mo/γ-Al_2O_3 catalysts. A clear evolution in product composition is observed upon modification of the catalyst with active metal species. The γ-Al_2O_3 catalyst produces a liquid fraction dominated by hydrocarbons (~67%), accompanied by a relatively high proportion of oxygenated compounds, particularly carboxylic acids (~15%) and esters (~11%). This distribution reflects the limited intrinsic deoxygenation capability of bare γ-Al_2O_3, where acid-catalyzed cracking and partial decarboxylation occur but remain insufficient to fully remove oxygen functionalities from long-chain fatty acids. Similar behavior has been reported for γ-Al_2O_3-supported systems lacking active metal sites, where oxygenated intermediates persist in the liquid phase under inert conditions [9,51].

The Ni/γ-Al_2O_3 catalyst markedly shifts the liquid composition toward relative hydrocarbon content, reaching approximately 85%. Concurrently, the fractions of carboxylic acids and esters are substantially reduced to below 10% and 5%, respectively. This result indicates that NiO sites effectively promote deoxygenation pathways, particularly decarboxylation and decarbonylation, enabling efficient oxygen removal without external hydrogen. Ni-based catalysts are well known to favor C–O bond scission and COx elimination during the deoxygenation of triglycerides and fatty acids, producing hydrocarbon-rich liquid products under inert atmospheres [20,32,52].

A similar hydrocarbon dominance is observed for Mo/γ-Al_2O_3, with relative hydrocarbon content accounting for approximately 85% of the liquid product. Compared with Ni/γ-Al_2O_3, this catalyst retains slightly higher fractions of oxygenated species, such as acids and cyclic oxygenates. This behavior can be attributed to the oxophilic nature of Mo species, which stabilize oxygen-containing intermediates on the catalyst surface. Previous studies have shown that Mo-based catalysts can facilitate deoxygenation but may also promote secondary reactions such as condensation and cyclization, particularly when MoOx domains or aluminum molybdate species are present, resulting in incomplete oxygen removal [31,32].

The bimetallic Ni–Mo/γ-Al_2O_3 catalyst exhibits the highest relative hydrocarbon content, reaching approximately 91%, while oxygenated compounds are reduced to minor residual fractions. This superior performance highlights the synergistic interaction between Ni and Mo species, where Ni provides highly active sites for C–O bond cleavage and CO/CO_2 release, while Mo modulates surface acidity and the adsorption strength of reaction intermediates, thereby suppressing the accumulation of oxygenated by-products. Such synergistic effects in Ni–Mo systems have been widely reported in deoxygenation and hydroprocessing studies, where balanced metal functionalities enhance relative hydrocarbon content while minimizing undesired oxygenates [17,30,44].

3.5.4. Carbon-number distribution and reaction preference

Fig. 11**b** shows the carbon-number selectivity profile of hydrocarbon products in the C7–C20 range obtained from the deoxygenation of washed waste corn oil over different catalysts. The distribution of carbon chains provides insight into the dominant reaction pathways, including decarboxylation, decarbonylation, and secondary cracking

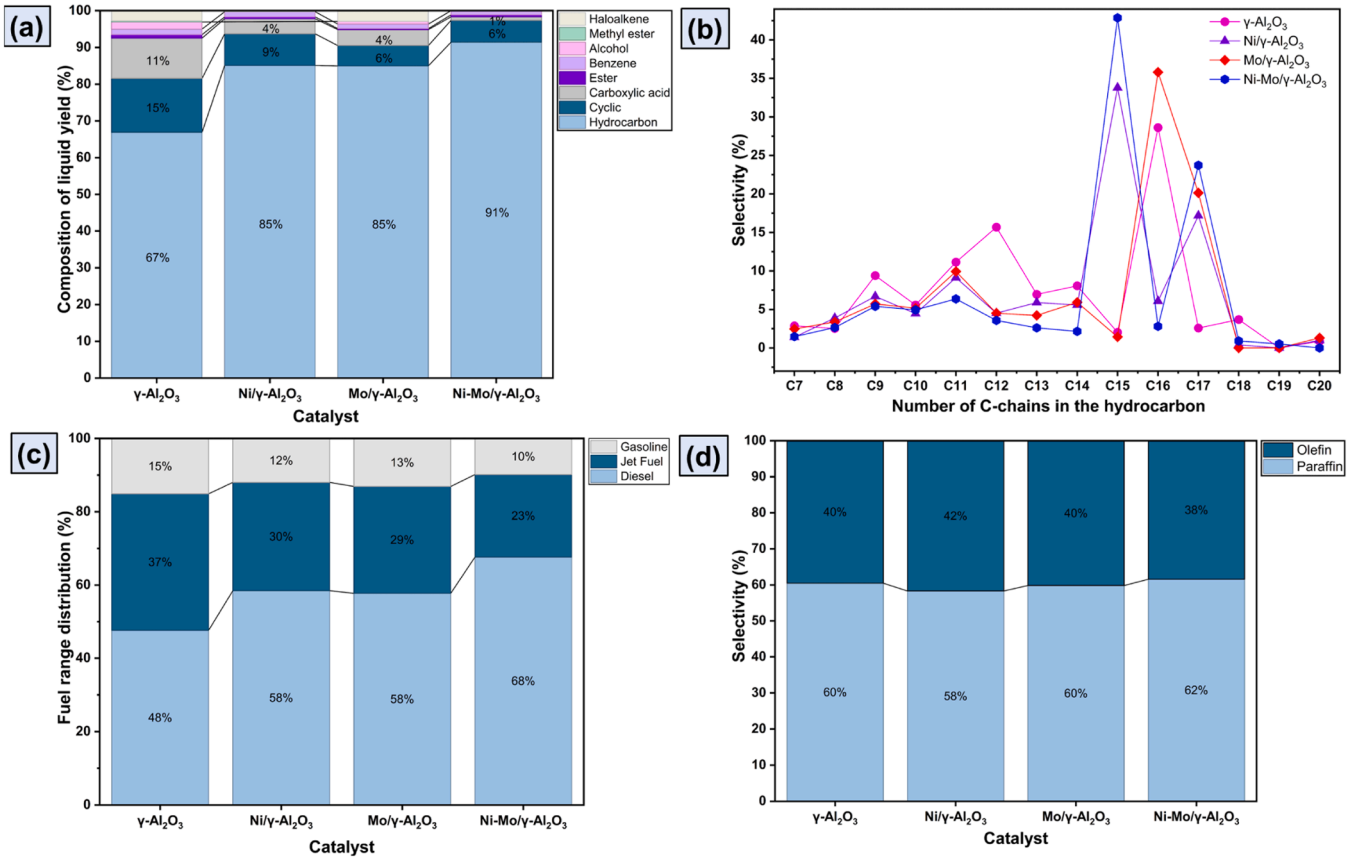

Fig. 11. Product composition and fuel-range distribution from deoxygenation of washed waste corn oil over different catalysts: (a) composition of liquid product, (b) carbon-number selectivity profile across C7–C20, (c) fuel-range partitioning into diesel, jet fuel, and gasoline fractions, and (d) paraffin versus olefin selectivity. Data presented for γ-Al_2O_3, Ni/γ-Al_2O_3, Mo/γ-Al_2O_3, and Ni–Mo/γ-Al_2O_3.

reactions. For γ-Al_2O_3, the product distribution is relatively broad, with noticeable selectivity toward lighter hydrocarbons in the C9–C13 range and only moderate formation of C15–C17 species. This behavior reflects the predominance of acid-catalyzed cracking and partial deoxygenation over γ-Al_2O_3, where the absence of metal sites limits efficient C–O bond cleavage and promotes non-selective chain scission. Similar broad carbon-number distributions with enhanced light fractions have been reported for γ-Al_2O_3-based catalysts under inert deoxygenation conditions [9,51].

The introduction of Ni significantly shifts the selectivity toward the diesel-range hydrocarbons, particularly C15 and C17 species. The pronounced peak around C15–C17 for Ni/γ-Al_2O_3 indicates that decarboxylation and decarbonylation of C18 fatty acids proceed efficiently, producing hydrocarbons with slightly shorter carbon chains. This trend is consistent with the well-established role of Ni in facilitating C–O bond cleavage and COx elimination without extensive hydrogenation, resulting in the selective formation of C15–C17 hydrocarbons under hydrogen-free conditions [18,20].

The Mo/γ-Al_2O_3 catalyst also enhances selectivity toward C15–C17 hydrocarbons but exhibits a slightly broader distribution compared with Ni/γ-Al_2O_3, with increased formation of C16 species. This behavior suggests that MoO_3 species stabilize oxygenated intermediates and promote deoxygenation pathways that partially preserve the carbon backbone while still allowing some secondary cracking. Previous studies on MoO_3-based deoxygenation catalysts have reported similar distributions, where MoOx domains favor selective oxygen removal but may also induce secondary reactions depending on metal dispersion and surface acidity. [31,32].

The bimetallic Ni–Mo/γ-Al_2O_3 catalyst exhibits the most pronounced selectivity within the C15–C17 range, with a dominant peak centered around C15. This distribution closely matches the theoretical prediction for the deoxygenation of C18 fatty acids via decarboxylation and decarbonylation pathways. The sharper selectivity profile indicates a synergistic interaction between NiO and MoO_3, where Ni provides highly active sites for C–O bond scission while Mo modulates the adsorption strength of reaction intermediates and suppresses excessive cracking. Such synergistic effects in Ni–Mo systems have been widely reported to enhance selectivity toward diesel-range hydrocarbons while minimizing the formation of lighter gases and heavier residues [30,53].

3.5.5. *Fuel-range selectivity*

Fig. 11**c** shows the distribution of liquid hydrocarbons into gasoline (C7–C9), jet fuel (C10–C14), and diesel (C15–C20) fractions obtained from the deoxygenation of washed waste corn oil over different catalysts. This carbon-number classification enables a direct evaluation of fuel quality and reflects the extent to which carbon-chain preservation is maintained relative to secondary cracking during the reaction. Over γ-Al_2O_3, the diesel fraction (C15–C20) accounts for approximately 48%, while the jet fuel (C10–C14) and gasoline (C7–C9) fractions reach 37% and 15%, respectively. This product distribution indicates that deoxygenation on bare γ-Al_2O_3 is accompanied by extensive acid-catalyzed cracking, which shortens carbon chains and shifts the distribution toward lighter fuels. The limited diesel selectivity highlights the inability of γ-Al_2O_3 to selectively convert long-chain fatty acids into diesel-range hydrocarbons without significant carbon loss, as commonly reported for γ-Al_2O_3-based systems lacking active metal sites [9].

Ni/γ-Al_2O_3 shows a pronounced increase in diesel selectivity, with the C15–C20 fraction rising to about 58%, while the jet fuel and gasoline fractions decrease to 30% and 12%, respectively. This shift demonstrates that Ni effectively suppresses excessive cracking and promotes selective deoxygenation of C18 fatty acids via decarboxylation and decarbonylation pathways, thereby preserving the carbon chain and improving carbon efficiency. Such behavior is consistent with numerous studies reporting Ni as an efficient metal for hydrogen-free deoxygenation with high selectivity toward diesel-range hydrocarbons [20,44].

The Mo/γ-Al_2O_3 catalyst also yields a high diesel fraction of approximately 58% but retains a broader fuel-range distribution, with 29% jet fuel and 13% gasoline. This broader distribution suggests that while MoO_3 facilitates oxygen removal, it also allows partial secondary cracking and carbon-chain rearrangement. The oxophilic nature and acidity associated with MoOx or molybdate-related species have been reported to stabilize oxygenated intermediates and promote secondary reactions, resulting in a less sharply defined diesel fraction compared with Ni-based catalysts [28,44].

The best performance is observed for the bimetallic Ni–Mo/γ-Al_2O_3 catalyst, which delivers the highest diesel selectivity, reaching approximately 68%, while the jet fuel and gasoline fractions decrease to 23% and 10%, respectively. The dominance of diesel-range hydrocarbons indicates a strong synergistic interaction between NiO and MoO_3, where NiO provides highly active sites for C–O bond cleavage and COx elimination, while MoO_3 modulates surface acidity and the adsorption strength of reaction intermediates to suppress overcracking. This synergy enables effective control of reaction pathways and maximizes the formation of C15–C20 hydrocarbons characteristic of green diesel [30,31,44].

The XRD analysis reveals distinct differences in the distribution of Mo-containing phases between the monometallic and bimetallic catalysts. In the Mo/γ-Al_2O_3 catalyst, the diffraction pattern shows clear reflections corresponding to aluminum molybdate ($Al_2(MoO_4)_3$), indicating strong interactions between Mo species and the γ-Al_2O_3 support during calcination. The formation of $Al_2(MoO_4)_3$ suggests that Mo species become anchored to the γ-Al_2O_3 framework through Mo–O–Al linkages. Although such molybdate species can enhance the structural stability of Mo on γ-Al_2O_3, their formation may reduce the availability of dispersed MoO_x surface sites, which are generally considered more active for oxygen removal reactions [30].

In contrast, the Ni–Mo/γ-Al_2O_3 catalyst exhibits more pronounced reflections corresponding to MoO_3, while the aluminum molybdate phase is not detected. This observation indicates that Mo species in the bimetallic catalyst remain predominantly as dispersed oxide domains rather than being incorporated into the γ-Al_2O_3 framework as molybdate phases. The presence of Ni species likely modifies the interaction between MoO_x and the support, thereby suppressing extensive molybdate formation and promoting more favorable dispersion of Mo-containing species on the catalyst surface. Such behavior is commonly attributed to interactions between Ni and Mo species, which can alter the distribution of MoO_x clusters on the γ-Al_2O_3 surface and limit their direct reaction with the support during calcination. Similar cooperative interactions between Ni and Mo species on γ-Al_2O_3-supported catalysts have been widely reported to enhance catalytic activity through synergistic effects in hydroprocessing and related reactions [24,25]. Consistent with these structural characteristics, the Mo/γ-Al_2O_3 catalyst yields 35.29% liquid product with 58% diesel-range selectivity, whereas the Ni–Mo/γ-Al_2O_3 catalyst achieves the highest performance with a liquid yield of 39.66% and diesel selectivity of 68%. These results indicate that maintaining Mo species as dispersed MoO_3 domains, together with cooperative interactions between Ni and Mo species, provides accessible active sites and enhances catalytic activity during the deoxygenation reaction.

The decrease in surface area and pore volume after metal incorporation indicates partial occupation of the mesoporous γ-Al_2O_3 framework by NiO and MoO_3 species within the pore network. As summarized in Table 2, the pristine γ-Al_2O_3 support exhibits the highest textural properties with a surface area of 133.20 $m^2\ g^{-1}$ and a pore volume of 0.278 $cm^3\ g^{-1}$, whereas metal incorporation reduces these values to 106.62 $m^2\ g^{-1}$ and 0.230 $cm^3\ g^{-1}$ for Ni/γ-Al_2O_3, 56.44 $m^2\ g^{-1}$ and 0.103 $cm^3\ g^{-1}$ for Mo/γ-Al_2O_3, and 81.36 $m^2\ g^{-1}$ and 0.150 $cm^3\ g^{-1}$ for Ni–Mo/γ-Al_2O_3. Despite this decrease, all catalysts retain mesoporous structures with average pore diameters ranging from 6.98 to 7.71 nm, which remain sufficiently large to accommodate bulky triglyceride molecules and facilitate their diffusion toward catalytic active sites. Triglyceride molecules typically have molecular dimensions of

approximately 2–3 nm, and mesopores larger than 5 nm are generally considered adequate to promote their diffusion within catalyst pore networks [39]. Therefore, although metal loading reduces surface area and pore volume, the remaining mesoporous channels remain sufficient to support mass transfer of triglycerides and reaction intermediates during the deoxygenation reaction [9].

Furthermore, these results indicate that catalytic performance is governed not only by textural properties but also by the nature and distribution of active metal sites. Although the γ-Al_2O_3 support possesses the highest SBET (133.20 m^2 g^{-1}) and pore volume (0.278 cm^3 g^{-1}), it produces a relatively low liquid yield of 32–33% with limited hydrocarbon formation. In contrast, the Ni–Mo/γ-Al_2O_3 catalyst, despite its lower textural properties (81.36 m^2 g^{-1}; 0.150 cm^3 g^{-1}), exhibits superior catalytic performance with a liquid yield of 39.66%, hydrocarbon content of 91%, and diesel selectivity of 68%. This behavior highlights the importance of synergistic interactions between NiO and MoO_3 species, which create effective active sites for C–O bond cleavage and hydrocarbon formation, while the preserved mesoporous channels ensure adequate mass transfer during the deoxygenation process [9,54].

3.5.6. Paraffin–olefin distribution

Fig. 11**d** presents the paraffin and olefin selectivity of liquid products obtained from the deoxygenation of washed waste corn oil over γ-Al_2O_3, Ni/γ-Al_2O_3, Mo/γ-Al_2O_3, and Ni–Mo/γ-Al_2O_3 catalysts. The paraffin–olefin ratio is an important indicator of hydrogen-transfer capability, hydrocarbon saturation level, and fuel stability. Over γ-Al_2O_3, the liquid product consists of approximately 60% paraffins and 40% olefins. The relatively high olefin content reflects the absence of active metal sites capable of promoting hydrogen-transfer reactions, resulting in unsaturated hydrocarbons formed primarily via acid-catalyzed cracking and decarboxylation. Olefin-rich products are commonly observed for γ-Al_2O_3-based catalysts under inert conditions and are typically associated with lower fuel stability and a higher tendency toward polymerization and coke formation [46].

For Ni/γ-Al_2O_3, the paraffin fraction reaches about 58%, while the olefin fraction remains close to 40%. Although the increase in paraffin selectivity compared with γ-Al_2O_3 is modest, the presence of NiO clearly facilitates in situ hydrogen transfer reactions. Hydrogen generated during decarbonylation and decarboxylation can be utilized to partially hydrogenate olefinic intermediates, leading to a higher degree of saturation without external hydrogen supply. Such behavior is characteristic of Ni-based catalysts during hydrogen-free deoxygenation of lipid-derived feedstocks [40]. A similar paraffin–olefin distribution is observed for Mo/γ-Al_2O_3, with approximately 60% paraffins and 40% olefins. This result indicates that MoO_3 species contribute to deoxygenation but possess limited hydrogen-transfer capability compared with NiO. MoOx or molybdate-related species tend to stabilize oxygenated and unsaturated intermediates on the catalyst surface, which can hinder complete olefin saturation and maintain a relatively high olefin fraction in the liquid product [28].

The highest paraffin selectivity is achieved over the bimetallic Ni–Mo/γ-Al_2O_3 catalyst, yielding about 62% paraffins and 38% olefins. This improvement demonstrates a synergistic interaction between NiO and MoO_3, where NiO provides effective hydrogen-transfer and olefin-saturation functionality, while MoO_3 modulates surface acidity and adsorption strength, suppressing secondary reactions that generate unsaturated hydrocarbons. The resulting paraffin-rich product composition indicates enhanced fuel stability and is consistent with the superior green diesel quality obtained over Ni–Mo catalysts reported in previous studies [55].

3.5.7. ATR-FTIR analysis of feedstock and liquid products

Fig. 12 shows the ATR-FTIR spectra of the waste corn oil feedstock and the liquid products obtained over γ-Al_2O_3, Ni/γ-Al_2O_3, Mo/γ-Al_2O_3, and Ni–Mo/γ-Al_2O_3 catalysts. The waste corn oil feedstock exhibits intense absorption bands at 2923 and 2852 cm^{-1}, attributed to asymmetric and symmetric stretching vibrations of aliphatic –CH_2– groups from triglyceride chains. A strong band at 1711 cm^{-1} corresponds to C═O stretching of ester functional groups, while the bands at 1260, 1096, and 1021 cm^{-1} are assigned to C–O stretching vibrations of ester linkages. Additionally, the bands at 1461 cm^{-1} (CH_2 bending vibrations) and 721 cm^{-1} (long-chain –$(CH_2)n$– rocking) confirm the presence of long aliphatic chains characteristic of vegetable oil feedstocks [56].

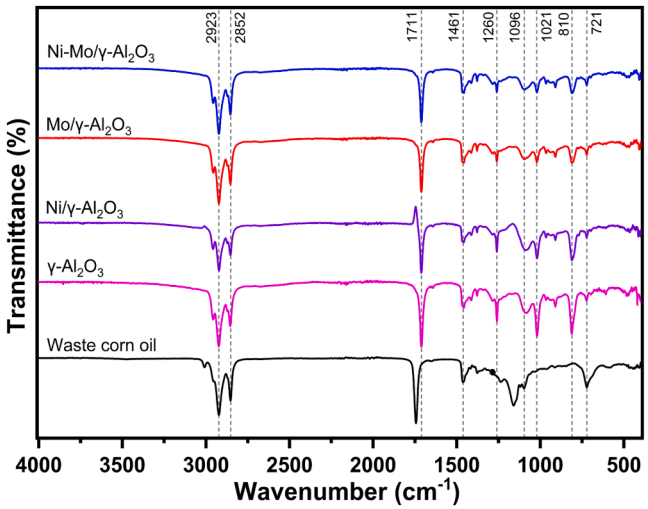

Fig. 12. ATR-FTIR spectra of feedstock and liquid product deoxygenation reaction.

The liquid product obtained over γ-Al_2O_3 shows only a slight reduction in the intensity of the ester-related bands at 1711, 1260, 1096, and 1021 cm^{-1}, indicating limited deoxygenation activity. The persistence of these oxygenated functional groups suggests that γ-Al_2O_3 mainly promotes thermal cracking or adsorption without effectively removing oxygen from triglyceride molecules. The aliphatic C–H stretching bands at 2923 and 2852 cm^{-1} remain prominent, reflecting the dominance of long-chain hydrocarbon structures with minimal chemical transformation [11].

The liquid product over Ni/γ-Al_2O_3 exhibits a noticeable decrease in the intensity of the carbonyl band at 1711 cm^{-1}, accompanied by a reduction of the C–O stretching bands at 1260, 1096, and 1021 cm^{-1}. These spectral changes indicate partial removal of oxygenated functionalities through decarboxylation and decarbonylation pathways. Meanwhile, the strong retention of aliphatic C–H stretching bands at 2923 and 2852 cm^{-1}, together with the band at 721 cm^{-1}, confirms the formation of long-chain hydrocarbon products [57].

For Mo/γ-Al_2O_3, the ester-related band at 1711 cm^{-1} is further weakened compared to Ni/γ-Al_2O_3, while the C–O bands at 1260 and 1096 cm^{-1} remain detectable. This suggests that Mo-based catalysts favor the formation of oxygenated intermediates, such as phenolics or ethers, during deoxygenation. The appearance of the band at 810 cm^{-1}, associated with out-of-plane C–H bending of substituted aromatic rings, indicates the formation of aromatic structures, which may act as intermediates or precursors to coke [28].

The liquid product obtained over Ni–Mo/γ-Al_2O_3 shows the most pronounced transformation relative to the feedstock. The carbonyl band at 1711 cm^{-1} is significantly suppressed, and the C–O stretching bands at 1260, 1096, and 1021 cm^{-1} are markedly reduced, indicating an advanced deoxygenation process. The dominance of aliphatic C–H stretching bands at 2923 and 2852 cm^{-1}, along with strong bands at 1461 and 721 cm^{-1}, confirms the formation of long-chain paraffinic hydrocarbons. The relatively weak intensity of the aromatic-related band at 810 cm^{-1} suggests that, although some aromatic species are formed, the liquid product is predominantly composed of saturated hydrocarbons [55].

3.6. Catalyst reproducibility, reusability, and stability of Ni–Mo/γ-Al_2O_3

The reusability and stability of the Ni–Mo/γ-Al_2O_3 catalyst were evaluated to assess its ability to maintain catalytic activity during repeated deoxygenation reactions. The experiments were performed using the same catalyst over consecutive reaction cycles under identical conditions in a semi-batch reactor. Prior to the reusability study, catalytic reproducibility was verified through four independent reactions using fresh catalyst. As shown in Fig. 13**(a)**, the liquid yield obtained from these experiments remained consistent, ranging from 39.66% to 40.61%, indicating good reproducibility and confirming that the activity variations observed during the reusability test were not caused by experimental variability

The reusability test was subsequently carried out over four consecutive cycles without catalyst regeneration. After each cycle, the catalyst was recovered by filtration, washed with n-hexane to remove residual reactants and heavy products, and dried at 110 °C for 12 h before reuse. As illustrated in Fig. 13**(b),** the liquid yield gradually decreased from 39.66% in the first cycle to 37.42%, 35.34%, and 33.32% in the second to fourth cycles. The catalyst retained 94.35%, 89.11%, and 84.01% of its initial activity in cycles two to four, corresponding to a cumulative activity loss of about 6.34 %age points (≈15.99%). The gradual decline (~2% per cycle) suggests progressive catalyst deactivation, commonly associated with the accumulation of carbonaceous species or heavy products that partially block active sites.

This behavior is supported by thermogravimetric analysis of the spent catalyst (Fig. 9), which shows a total mass loss of approximately 11.8 wt% attributed to deposited carbon species. To place these results in context, similar deactivation trends have been reported for other non-noble metal catalysts used in deoxygenation reactions. Shi et al. (2023) reported that the conversion over Ni/MgO–Al_2O_3 catalysts decreased from 100% to 88.06% after four cycles, while the hydrocarbon content declined from 95.12% to 71.63% [49]. Likewise, Wang et al. (2023) observed a decrease in conversion from 100% to 86.27% and hydrocarbon yield from 97.72% to 74.29% for Ce–Mo/Al-MCM−41 catalysts after four cycles [48].

3.7. Deoxygenation reaction mechanism

The proposed deoxygenation mechanism is illustrated in Fig. 14, which depicts the transformation of linoleic acid as a representative major fatty acid present in waste corn oil (Table S1) into various hydrocarbon products through several catalytic reaction pathways. Linoleic acid molecules are initially adsorbed on the catalyst surface and activated at the carboxyl group (–COOH). Under an inert N_2 atmosphere without external hydrogen supply, oxygen removal primarily proceeds through two main pathways, namely decarboxylation (DCO_2) and decarbonylation (DCO) [1,32]. In the decarboxylation pathway, bond cleavage occurs at the C–C bond between the carboxyl carbon and the α-carbon of the fatty acid chain, releasing the carboxyl group as CO_2 [1, 58]. This process forms unsaturated hydrocarbon fragments that subsequently undergo limited hydrogenation on the catalyst surface, producing saturated hydrocarbons in the form of alkanes [58]. In contrast, the decarbonylation pathway involves cleavage of the C–O bond in the carbonyl group, generating CO and H_2O as by-products. The resulting hydrocarbon fragments then undergo partial hydrogenation or stabilization on the catalyst surface, leading to the formation of alkanes as the final products. These two pathways are generally dominant in hydrogen-free systems since they do not require a large hydrogen supply for oxygen removal [1,32].

In addition to these primary pathways, Fig. 14 also illustrates several secondary reactions that may occur during the deoxygenation process. The CO and H_2O generated from the decarbonylation pathway can further react through the water–gas shift reaction ($CO + H_2O \rightleftharpoons CO_2 + H_2$), producing in situ hydrogen, which can participate in limited hydrogenation steps to convert olefins into paraffins and stabilize hydrocarbon intermediates [1]. Furthermore, long-chain hydrocarbons formed from the DCO_2 and DCO pathways may undergo secondary reactions such as cracking through C–C bond cleavage, producing shorter hydrocarbon chains [1]. These intermediates may also undergo cyclization and dehydrogenation, forming cyclic and aromatic compounds at elevated reaction temperatures. The hydrodeoxygenation (HDO) pathway is also included in the proposed mechanism as a minor route involving hydrogenation of oxygenated intermediates followed by the removal of oxygen as H_2O [1]. However, because the reaction is conducted under an N_2 atmosphere without external hydrogen supply, the contribution of this pathway is expected to be very limited and likely originates only from in situ hydrogen generated via the water–gas shift reaction or the reforming of oxygenated intermediates. Therefore, the oxygen removal in this system is mainly governed by decarboxylation and decarbonylation, while hydrogen formed from secondary reactions only contributes to limited hydrogenation that stabilizes the resulting hydrocarbon products [1,32].

4. Conclusion

The systematic comparison of γ-Al_2O_3, Ni/γ-Al_2O_3, Mo/γ-Al_2O_3, and Ni–Mo/γ-Al_2O_3 catalysts under hydrogen-free conditions demonstrates that catalyst composition plays a decisive role in governing structural properties, active-site distribution, and deoxygenation selectivity. Metal

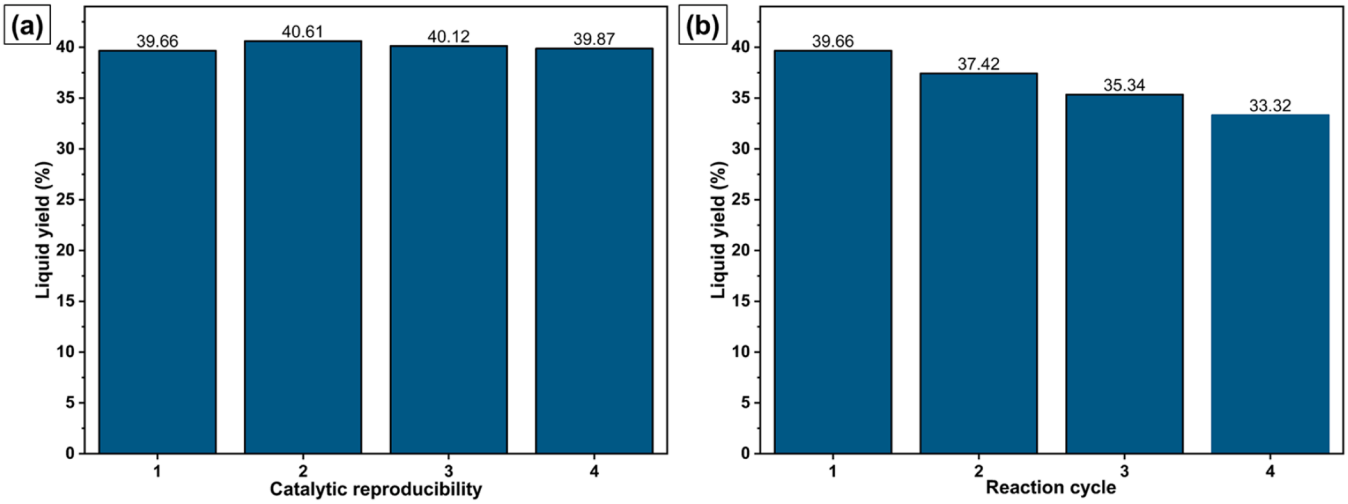

Fig. 13. Catalytic reproducibility of Ni–Mo/γ-Al_2O_3 catalyst (a), Reusability and stability of Ni–Mo/γ-Al_2O_3 over four reaction cycles (b).

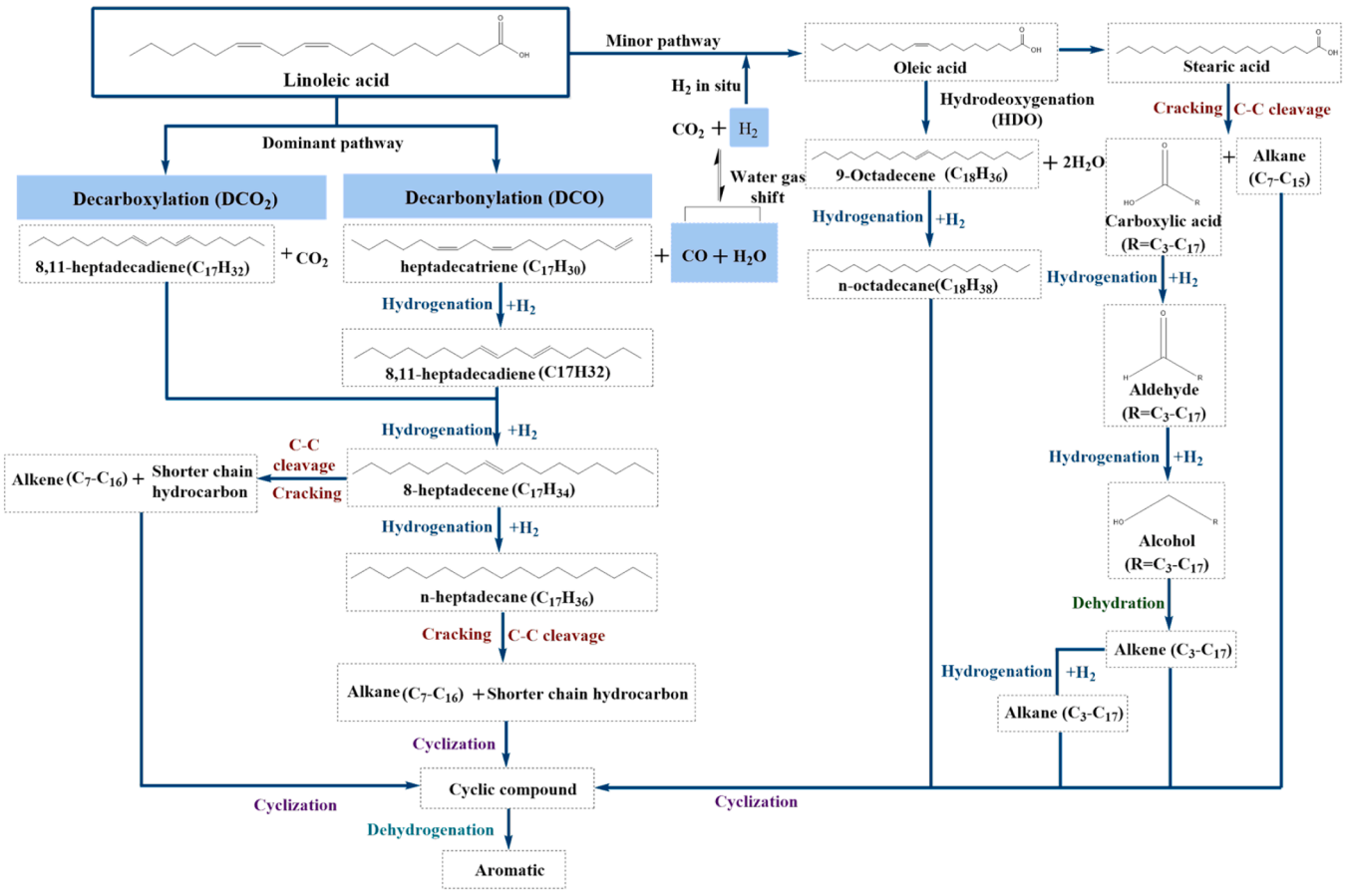

Fig. 14. Proposed reaction pathways for linoleic acid deoxygenation under hydrogen-free conditions.

impregnation modifies the surface chemistry and porosity of the γ-Al_2O_3 support, thereby influencing oxygen-removal pathways and the preservation of hydrocarbon chains during catalytic conversion. Among the investigated systems, the bimetallic Ni–Mo/γ-Al_2O_3 catalyst exhibits the most favorable catalytic performance, reflecting a synergistic interaction between NiO and MoO_3 species that promotes efficient C–O bond cleavage while moderating secondary cracking and coke formation. The dominant C18 fatty acid composition of the waste corn oil feedstock further facilitates selective transformation into hydrocarbons within the diesel range (C15–C20). These findings establish a clear structure–performance relationship between catalyst composition and deoxygenation selectivity. Overall, this study demonstrates that controlled Ni–Mo interfacial design on γ-Al_2O_3, combined with a C18-rich feedstock, provides an effective catalytic strategy for sustainable diesel-range hydrocarbon production under hydrogen-free conditions.

Data statement

All data supporting the findings of this article are contained within the paper.

CRediT authorship contribution statement

Susi Nurul Khalifah: Writing – review & editing, Validation, Supervision, Methodology, Conceptualization. **Saidun Fiddaroini:** Writing – review & editing, Supervision, Data curation, Conceptualization. **Moh. Nadhif Mauluddin:** Visualization, Software, Investigation, Formal analysis. **A. Ghanaim Fasya:** Writing – review & editing, Validation, Supervision. **Muhammad Falila Izzuddin Haqq:** Writing – original draft, Investigation, Formal analysis. **Muhammad Naufal Alhilmy:** Writing – original draft, Investigation, Formal analysis. **Karisma Pradina Putri:** Writing – original draft, Visualization, Methodology, Investigation, Formal analysis, Conceptualization.

Declaration of Generative AI and AI-assisted technologies in the writing process

During the preparation of this manuscript, the authors used ChatGPT to refine the English and improve readability.

Declaration of Competing Interest

The authors declare that they have no known competing financial interests or personal relationships that could have appeared to influence the work reported in this paper.

Appendix A. Supporting information

Supplementary data associated with this article can be found in the online version at doi:10.1016/j.nxmate.2026.101966.

References

[1] B.P. Pattanaik, R.D. Misra, Effect of reaction pathway and operating parameters on the deoxygenation of vegetable oils to produce diesel range hydrocarbon fuels: a review, Renew. Sustain. Energy Rev. 73 (Jun. 2017) 545–557, https://doi.org/10.1016/j.rser.2017.01.018.
[2] S. Sorrell, Reducing energy demand: a review of issues, challenges and approaches, Renew. Sustain. Energy Rev. 47 (Jul. 2015) 74–82, https://doi.org/10.1016/j.rser.2015.03.002.
[3] S. Lucantonio, A. Di Giuliano, L. Rossi, K. Gallucci, Green diesel production via deoxygenation process: a review, Energies 16 (2) (Jan. 2023) 844, https://doi.org/10.3390/en16020844.

[4] 'Transforming our world: the 2030 Agenda for Sustainable Development | Department of Economic and Social Affairs'. Accessed: Feb. 11, 2026. [Online]. Available: ⟨https://sdgs.un.org/2030agenda⟩.

[5] Z. Rahmawati, et al., Selectivity of reaction pathways for green diesel production towards biojet fuel applications, RSC Adv. 13 (20) (May 2023) 13698–13714, https://doi.org/10.1039/D3RA02281A.

[6] G. Knothe, Biodiesel and renewable diesel: a comparison, Prog. Energy Combust. Sci. 36 (3) (Jun. 2010) 364–373, https://doi.org/10.1016/j.pecs.2009.11.004.

[7] G.W. Huber, S. Iborra, A. Corma, Synthesis of transportation fuels from biomass: chemistry, catalysts, and engineering, Chem. Rev. 106 (9) (Sep. 2006) 4044–4098, https://doi.org/10.1021/cr068360d.

[8] N. Asikin-Mijan, et al., Towards sustainable green diesel fuel production: advancements and opportunities in acid-base catalyzed H2-free deoxygenation process, Catal. Commun. 182 (Sep. 2023) 106741, https://doi.org/10.1016/j.catcom.2023.106741.

[9] D. Kubička, L. Kaluža, Deoxygenation of vegetable oils over sulfided Ni, Mo and NiMo catalysts, ' Appl. Catal. Gen. 372 (2) (Jan. 2010) 199–208, https://doi.org/10.1016/j.apcata.2009.10.034.

[10] *Transforming our world: the 2030 Agenda for Sustainable Development: draft resolution referred to the United Nations summit for the adoption of the post-2015 development agenda by the General Assembly at its 69th session*. New York: UN, 18. Accessed: Feb. 10, 2026. [Online]. Available: ⟨https://digitallibrary.un.org/record/803352⟩.

[11] R.A. Moreau, Corn Oil. Vegetable oils in food technology, John Wiley & Sons, Ltd, 2011, pp. 273–289, https://doi.org/10.1002/9781444339925.ch10.

[12] S. Feng, et al., Comprehensive evaluation of chemical composition and health-promoting effects with chemometrics analysis of plant derived edible oils, Food Chem. X 14 (Jun. 2022) 100341, https://doi.org/10.1016/j.fochx.2022.100341.

[13] D. Prangklang, D. Tumnantong, B. Yoosuk, C. Ngamcharussrivichai, P. Prasassarakich, Selective deoxygenation of waste cooking oil to diesel-like hydrocarbons using supported and unsupported NiMoS2 catalysts, ACS Omega 8 (43) (Oct. 2023) 40921–40933, https://doi.org/10.1021/acsomega.3c06188.

[14] G. Garbarino, T.K. Phung, G. Pampararo, P. Riani, G. Busca, Modification of the properties of γ-alumina as a support for nickel and molybdate catalysts by addition of silica, Catal. Today 378 (Oct. 2021) 57–64, https://doi.org/10.1016/j.cattod.2021.02.016.

[15] D. Kim, B. Choi, G. Park, K. Lee, D.-W. Lee, S. Jung, Effect of γ-Al2O3 characteristics on hydrogen production of Cu/γ-Al2O3 catalyst for steam reforming of dimethyl ether, Chem. Eng. Sci. 216 (Apr. 2020) 115535, https://doi.org/10.1016/j.ces.2020.115535.

[16] N. Krobkrong, V. Itthibenchapong, P. Khongpracha, K. Faungnawakij, Deoxygenation of oleic acid under an inert atmosphere using molybdenum oxide-based catalysts, Energy Convers. Manag 167 (Jul. 2018) 1–8, https://doi.org/10.1016/j.enconman.2018.04.079.

[17] E. Kordouli, L. Sygellou, C. Kordulis, K. Bourikas, A. Lycourghiotis, Probing the synergistic ratio of the NiMo/γ-Al2O3 reduced catalysts for the transformation of natural triglycerides into green diesel, Appl. Catal. B Environ. 209 (Jul. 2017) 12–22, https://doi.org/10.1016/j.apcatb.2017.02.045.

[18] N. Hongloi, P. Prapainainar, A. Seubsai, K. Sudsakorn, C. Prapainainar, Nickel catalyst with different supports for green diesel production, Energy 182 (Sep. 2019) 306–320, https://doi.org/10.1016/j.energy.2019.06.020.

[19] T.A. Zepeda, Ultrasonic-assistance influence on the impregnation method for high metal loading CoMo/Ti-HMS catalysts, ' Appl. Catal. Gen. 693 (Mar. 2025) 120135, https://doi.org/10.1016/j.apcata.2025.120135.

[20] M. Ameen, M.T. Azizan, A. Ramli, S. Yusup, B. Abdullah, The effect of metal loading over Ni/γ-Al2O3 and Mo/γ-Al2O3 catalysts on reaction routes of hydrodeoxygenation of rubber seed oil for green diesel production, Catal. Today 355 (Sep. 2020) 51–64, https://doi.org/10.1016/j.cattod.2019.03.028.

[21] M. Trueba, S.P. Trasatti, γ-alumina as a support for catalysts: a review of fundamental aspects, Eur. J. Inorg. Chem. 2005 (Sep. 2005) 3393–3403, https://doi.org/10.1002/ejic.200500348.

[22] S.N. Khalifah, S. Fiddaroini, D.U. Sholekhah, A.G. Salshabilla, A. Zakiyah, Comparative catalytic performance of mesoporous and microporous NaP zeolites synthesized from natural kaolin via hydrothermal and sonochemical methods for castor oil transesterification, Mater 10 (Jan. 2026) 101567, https://doi.org/10.1016/j.nxmate.2025.101567.

[23] Z. Li, et al., Sonochemical fabrication of inorganic nanoparticles for applications in catalysis, Ultrason. Sonochem. 71 (Mar. 2021) 105384, https://doi.org/10.1016/j.ultsonch.2020.105384.

[24] B. Behnejad, M. Abdouss, A. Tavasoli, Comparison of performance of Ni–Mo/γ-alumina catalyst in HDS and HDN reactions of main distillate fractions, Pet. Sci. 16 (3) (Jun. 2019) 645–656, https://doi.org/10.1007/s12182-019-0319-5.

[25] X. Li, et al., Effect of preparation method of NiMo/γ-Al2O3 on the FAME hydrotreatment to produce C15–C18 alkanes, Renew. Energy 193 (Jun. 2022) 1–12, https://doi.org/10.1016/j.renene.2022.03.115.

[26] X. Liu, L. Zhang, X. Zheng, Y. Zhang, D. He, Y. Luo, Highly dispersed Ni/Al2O3 catalysts for dry reforming of methane prepared by alkaline-induced adsorption process, Int. J. Hydrog. Energy 47 (72) (Aug. 2022) 30937–30949, https://doi.org/10.1016/j.ijhydene.2022.01.217.

[27] Y. Abdelbaki, et al., The nickel-support interaction as determining factor of the selectivity to ethylene in the oxidative dehydrogenation of ethane over nickel oxide/alumina catalysts, ' Appl. Catal. Gen. 623 (Aug. 2021) 118242, https://doi.org/10.1016/j.apcata.2021.118242.

[28] M.B.I. Chowdhury, Md Zakir Hossain, P.A. Charpentier, Reduction and structural modification of MoOx/γ-Al2O3 catalysts through acetic acid treatment for green diesel production from corn distiller's oil, Energy Convers. Manag 322 (Dec. 2024) 119135, https://doi.org/10.1016/j.enconman.2024.119135.

[29] R.A. Lucky, M.L. Balogun, W.U. Khan, S. Ahmed, M.S. Ba-Shammakh, M. M. Hossain, Ga2O3/La2O3-γAl2O3 catalysts for CO2-assisted propane oxidative dehydrogenation to propylene, ' Appl. Catal. Gen. 685 (Sep. 2024) 119890, https://doi.org/10.1016/j.apcata.2024.119890.

[30] P. Kumar, S.K. Maity, D. Shee, Role of NiMo Alloy and Ni species in the performance of NiMo/alumina catalysts for hydrodeoxygenation of stearic acid: a kinetic study, ACS Omega 4 (2) (Feb. 2019) 2833–2843, https://doi.org/10.1021/acsomega.8b03592.

[31] N. Hongloi, et al., Palm oil deoxygenation with glycerol as a hydrogen donor for renewable fuel production using nickel-molybdenum catalysts: the effect of support, Fuel Process. Technol. 270 (Jun. 2025) 108196, https://doi.org/10.1016/j.fuproc.2025.108196.

[32] R.E. Nugraha, et al., The mechanism of oleic acid deoxygenation to green diesel hydrocarbon using porous aluminosilicate catalysts, South Afr. J. Chem. Eng. 49 (Jul. 2024) 122–135, https://doi.org/10.1016/j.sajce.2024.04.009.

[33] M. Thommes, et al., Physisorption of gases, with special reference to the evaluation of surface area and pore size distribution (IUPAC Technical Report), Pure Appl. Chem. 87 (9–10) (Oct. 2015) 1051–1069, https://doi.org/10.1515/pac-2014-1117.

[34] S.L. Douvartzides, N.D. Charisiou, K.N. Papageridis, M.A. Goula, Green diesel: biomass feedstocks, production technologies, catalytic research, fuel properties and performance in compression ignition internal combustion engines, Energies 12 (5) (Jan. 2019) Art. no. 5, https://doi.org/10.3390/en12050809.

[35] G. Busca, The surface of transitional aluminas: a critical review, Catal. Today 226 (May 2014) 2–13, https://doi.org/10.1016/j.cattod.2013.08.003.

[36] L. Shi, Z. Zhang, R. Wang, C. Zhou, C. Sun, Study on ultrasound-assisted precipitation for preparing Ni/Al2O3 catalyst, Ultrason. Sonochem. 67 (Oct. 2020) 105107, https://doi.org/10.1016/j.ultsonch.2020.105107.

[37] Y. Wang, et al., Structure and reducibility of NiO-MoO3/γ-Al2O3 catalysts: effects of loading and molar ratio, J. Phys. Chem. C. 112 (44) (Nov. 2008) 17265–17271, https://doi.org/10.1021/jp800182j.

[38] A. Muñoz-Arjona, A. Ayala-Cortés, C.D. Stasi, D. Torres, J.L. Pinilla, I. Suelves, Catalytic hydrodeoxygenation of waste cooking oil into green diesel range hydrocarbons: from batch to continuous processing, Chem. Eng. J. 503 (Jan. 2025) 158303, https://doi.org/10.1016/j.cej.2024.158303.

[39] K.K. Ferreira, et al., Hydroprocessing of waste cooking oil to produce liquid fuels over Ni-Mo and Co-Mo supported on carbon nanotubes, Biomass-.-. Bioenergy 191 (Dec. 2024) 107480, https://doi.org/10.1016/j.biombioe.2024.107480.

[40] W.N.A. Wan Khalit, et al., One-pot decarboxylation and decarbonylation reaction of waste cooking oil over activated carbon supported nickel-zinc catalyst into diesel-like fuels, J. Anal. Appl. Pyrolysis 164 (Jun. 2022) 105505, https://doi.org/10.1016/j.jaap.2022.105505.

[41] Ł. Jęczmionek, K. Porzycka-Semczuk, Hydrodeoxygenation, decarboxylation and decarbonylation reactions while co-processing vegetable oils over NiMo hydrotreatment catalyst. Part II: thermal effects – experimental results, Fuel 128 (Jul. 2014) 296–301, https://doi.org/10.1016/j.fuel.2014.03.023.

[42] H. Li, M. Li, Y. Chu, F. Liu, H. Nie, Effect of different preparation methods of MoO3/Al2O3 catalysts on the existing states of Mo species and hydrodesulfurization activity, Fuel 116 (Jan. 2014) 168–174, https://doi.org/10.1016/j.fuel.2013.07.127.

[43] E. Kordouli, B. Pawelec, K. Bourikas, C. Kordulis, J.L.G. Fierro, A. Lycourghiotis, Mo promoted Ni-Al2O3 co-precipitated catalysts for green diesel production, Appl. Catal. B Environ. 229 (Aug. 2018) 139–154, https://doi.org/10.1016/j.apcatb.2018.02.015.

[44] X. Li, et al., Effect of preparation method of NiMo/γ-Al2O3 on the FAME hydrotreatment to produce C15–C18 alkanes, Renew. Energy 193 (Jun. 2022) 1–12, https://doi.org/10.1016/j.renene.2022.03.115.

[45] E. Furimsky, Catalytic hydrodeoxygenation, ' Appl. Catal. Gen. 199 (2) (Jun. 2000) 147–190, https://doi.org/10.1016/S0926-860X(99)00555-4.

[46] P.M. Mortensen, J.-D. Grunwaldt, P.A. Jensen, K.G. Knudsen, A.D. Jensen, 'A review of catalytic upgrading of bio-oil to engine fuels', Appl. Catal. Gen. 407 (1) (Nov. 2011) 1–19, https://doi.org/10.1016/j.apcata.2011.08.046.

[47] Ł. Jęczmionek, K. Porzycka-Semczuk, Hydrodeoxygenation, decarboxylation and decarbonylation reactions while co-processing vegetable oils over a NiMo hydrotreatment catalyst. Part I: Thermal effects – Theoretical considerations, Fuel 131 (Sep. 2014) 1–5, https://doi.org/10.1016/j.fuel.2014.04.055.

[48] J. Wang, et al., Highly stable Mo-based bimetallic catalysts for selective deoxygenation of oleic acid to fuel-like hydrocarbons, J. Environ. Chem. Eng. 11 (1) (Feb. 2023) 109104, https://doi.org/10.1016/j.jece.2022.109104.

[49] F. Shi, et al., Green diesel-like hydrocarbon production by H2-free catalytic deoxygenation of oleic acid via Ni/MgO-Al2O3 catalysts: effect of the metal loading amount, J. Environ. Chem. Eng. 11 (5) (Oct. 2023) 110520, https://doi.org/10.1016/j.jece.2023.110520.

[50] G. Knothe, Dependence of biodiesel fuel properties on the structure of fatty acid alkyl esters, Fuel Process. Technol. 86 (10) (Jun. 2005) 1059–1070, https://doi.org/10.1016/j.fuproc.2004.11.002.

[51] E. Santillan-Jimenez, M. Crocker, Catalytic deoxygenation of fatty acids and their derivatives to hydrocarbon fuels via decarboxylation/decarbonylation, J. Chem. Technol. Biotechnol. 87 (8) (Aug. 2012) 1041–1050, https://doi.org/10.1002/jctb.3775.

[52] S. Ding, et al., Catalytic hydrodeoxygenation of waste cooking oil and stearic acid over reduced nickel-basded catalysts, Catal. Commun. 149 (Jan. 2021) 106235, https://doi.org/10.1016/j.catcom.2020.106235.

[53] M. Ameen, M.T. Azizan, A. Ramli, S. Yusup, M.S. Alnarabiji, Catalytic hydrodeoxygenation of rubber seed oil over sonochemically synthesized Ni-Mo/

γ-Al2O3 catalyst for green diesel production, Ultrason. Sonochem. 51 (Mar. 2019) 90–102, https://doi.org/10.1016/j.ultsonch.2018.10.011.
[54] S. Bezergianni, A. Dimitriadis, Comparison between different types of renewable diesel, Renew. Sustain. Energy Rev. 21 (May 2013) 110–116, https://doi.org/10.1016/j.rser.2012.12.042.
[55] X. Cao, F. Long, Q. Zhai, P. Liu, J. Xu, J. Jiang, Enhancement of fatty acids hydrodeoxygenation selectivity to diesel-range alkanes over the supported Ni-MoOx catalyst and elucidation of the active phase, Renew. Energy 162 (Dec. 2020) 2113–2125, https://doi.org/10.1016/j.renene.2020.10.052.
[56] M.D. Guillén, N. Cabo, Characterization of edible oils and lard by fourier transform infrared spectroscopy. Relationships between composition and frequency of concrete bands in the fingerprint region, J. Am. Oil Chem. Soc. 74 (10) (Oct. 1997) 1281–1286, https://doi.org/10.1007/s11746-997-0058-4.
[57] S. Chen, J. Zeng, Z. Liao, H. Xie, G. Zhou, Controllable preparation of highly dispersed Ni/γ-Al2O3 catalyst for lipids hydrodeoxygenation to biofuel, J. Environ. Chem. Eng. 13 (5) (Oct. 2025) 117518, https://doi.org/10.1016/j.jece.2025.117518.
[58] I. Aziz, N. Saridewi, F. Febriyani, L. Adhani, Deoksigenasi katalitik metil ester asam lemak menjadi biohidrokarbon menggunakan katalis Cr2O3/Zeolit, ALCHEMY J. Penelit. Kim. 19 (2) (Sep. 2023) 170, https://doi.org/10.20961/alchemy.19.2.72521.170-176.
[59] B. Donnis, R.G. Egeberg, P. Blom, K.G. Knudsen, Hydroprocessing of bio-oils and oxygenates to hydrocarbons. Understanding the reaction routes, Top. Catal. 52 (3) (Apr. 2009) 229–240, https://doi.org/10.1007/s11244-008-9159-z.
[60] H. Knözinger, P. Ratnasamy, Catalytic aluminas: surface models and characterization of surface sites, Catal. Rev. 17 (1) (Jan. 1978) 31–70, https://doi.org/10.1080/03602457808080878.